Journal of Petrology, 2025, **66**, egaf015
https://doi.org/10.1093/petrology/egaf015
ADVANCE ACCESS PUBLICATION DATE 18 FEBRUARY 2025
Original Manuscript

Role of Chamber Replenishment in the Formation of the Merensky Reef and its Footwall Anorthosite

WILLIAM D. SMITH[1], HADRIEN HENRY[2], JUSSI S. HEINONEN[3,4], WOLFGANG D. MAIER[5], DUNCAN D. MUIR[5], SARAH-JANE BARNES[6] and JENS Ø. ANDERSEN[7]

[1]CSIRO Mineral Resources, 26 Dick Perry Avenue, Kensington, Perth, WA 6151, Australia
[2]Géosciences Environment Toulouse, Université de Toulouse III Paul Sabatier, 14 Avenue E. Belin, 31400 Toulouse, France
[3]Department of Geosciences and Geography, University of Helsinki, P.O. Box 64, 00014, Helsinki, Finland
[4]Geology and Mineralogy, Åbo Akademi University, Akademigatan 1, 20500 Åbo, Finland
[5]School of Earth & Environmental Sciences, Cardiff University, United Kingdom, CF10 3AT
[6]Sciences de la Terre, Université du Québec à Chicoutimi, 555 Boulevard de l'Universite, Quebec G7H 2B1, Canada
[7]Camborne School of Mines, University of Exeter, Penryn, United Kingdom, TR10 9EZ

*Corresponding author. E-mail: will.smith@csiro.au

The Merensky Reef of the Bushveld Complex represents a magmatic unconformity that some researchers attribute to chamber replenishment by relatively primitive magma. It is propounded that cumulate rocks in this chamber reacted with replenishing melt, as part of the process that ultimately produced chromitite stringers and reef-style platinum-group element mineralization. This study investigates as to whether chamber replenishment contributed to the formation of the Merensky Reef and its underlying anorthosite at the Rustenburg Platinum Mine in the western lobe of the Bushveld Complex.

At this location, the Merensky Reef is a coarse-grained pyroxenite bracketed by millimeter-scale chromitite stringers. This sequence is underlain by a centimeter-scale anorthosite which in turn is underlain by leuconorite. The leuconorite comprises normally zoned cumulus orthopyroxene with poikilitic rims (Mg_{80-79}) and cumulus plagioclase (An_{80-58}), where the latter defines a magmatic fabric indicative of gravitational settling of tabular crystals in a quiescent melt. The contact between leuconorite and anorthosite is marked by an increased abundance of late-stage accessory minerals, and the composition of poikilitic orthopyroxene at this horizon is consistent with trapped liquid shift. Plagioclase crystals in the anorthosite are variably zoned (An_{79-64}) and record a magmatic fabric that strengthens with proximity to the reef. This unit is traversed by sinuous networks of sulfides, pyroxenes, quartz, and very fine-grained chromite that terminate at the contact with the leuconorite. The lower chromitite hosts both amoeboidal and blocky chromite crystals that are enclosed by complexly zoned plagioclase oikocrysts in the lower two-thirds and by orthopyroxene oikocrysts in the upper third. The upper chromitite hosts only blocky crystals, similar to those in the upper portion of the lower chromitite. Microtextural characteristics of the amoeboidal crystals coupled with their propensity to host polymineralic inclusions, suggests that these were initially skeletal crystals that subsequently underwent dissolution-reprecipitation. There is no discernible chemical difference between amoeboidal and blocky crystals; however, accessory mineralogy and chromite chemistry imply that the upper portion of the lower chromitite and the upper chromitite experienced post-cumulus re-equilibration with evolved intercumulus silicate melt.

Our observations are consistent with the anorthosite being a restite of partially molten leuconoritic cumulates. This theory is supported by thermodynamic modelling that demonstrates that under certain conditions, replenishing melts can reconstitute noritic cumulates to anorthosite, troctolite, or feldspathic orthopyroxenite restites. The porosity generated during this process was exploited by downward percolating sulfide melt that displaced a proportionate amount of intercumulus silicate melt upward to the level of the nascent reef. Initially, these partial melts were likely relatively volatile-rich, triggering Cr-supersaturation at the cumulate-melt interface, and later became Cr-bearing with the consumption of poikilitic orthopyroxene and very fine-grained chromite.

Key words: Merensky Reef; Bushveld Complex; Element Mapping; Mineral Chemistry; EBSD; Magma Chamber Simulator

INTRODUCTION

The ∼ 2.056 Ga Bushveld Complex (Fig. 1) is the world's largest known layered mafic-ultramafic intrusion and host to the three most important platinum-group element (PGE) deposits, namely the UG2 chromitite, Platreef, and Merensky Reef (Eales and Cawthorn 1996; Maier *et al.* 2013; Cawthorn 2015; Kinnaird and McDonald 2018; Scoates *et al.* 2021; Smith and Maier 2021). The Merensky Reef can be traced across the extent of the Bushveld Complex, displaying remarkable uniformity in thickness and lithology (Vermaak 1976; Leeb du Toit 1986, Viljoen and Hieber 1986, Viljoen *et al.* 1986a; Viljoen 1999;; Roberts *et al.* 2007; Naldrett *et al.* 2009; Latypov *et al.* 2015; Grobler *et al.* 2019). It occurs within the *Upper Critical Zone*, which is characterized by interlayered units of chromitite, pyroxenite, norite, and anorthosite (Eales *et al.* 1988; Roberts *et al.* 2007). Since its discovery in 1924, the Merensky Reef has been the focus in research on the formation of stratiform horizons enriched in precious metals in layered mafic-ultramafic intrusions. Despite a century of investigations, the petrogenesis of such horizons remains controversial.

RECEIVED OCTOBER 15, 2024; **REVISED** FEBRUARY 7, 2025; **ACCEPTED** FEBRUARY 13, 2025

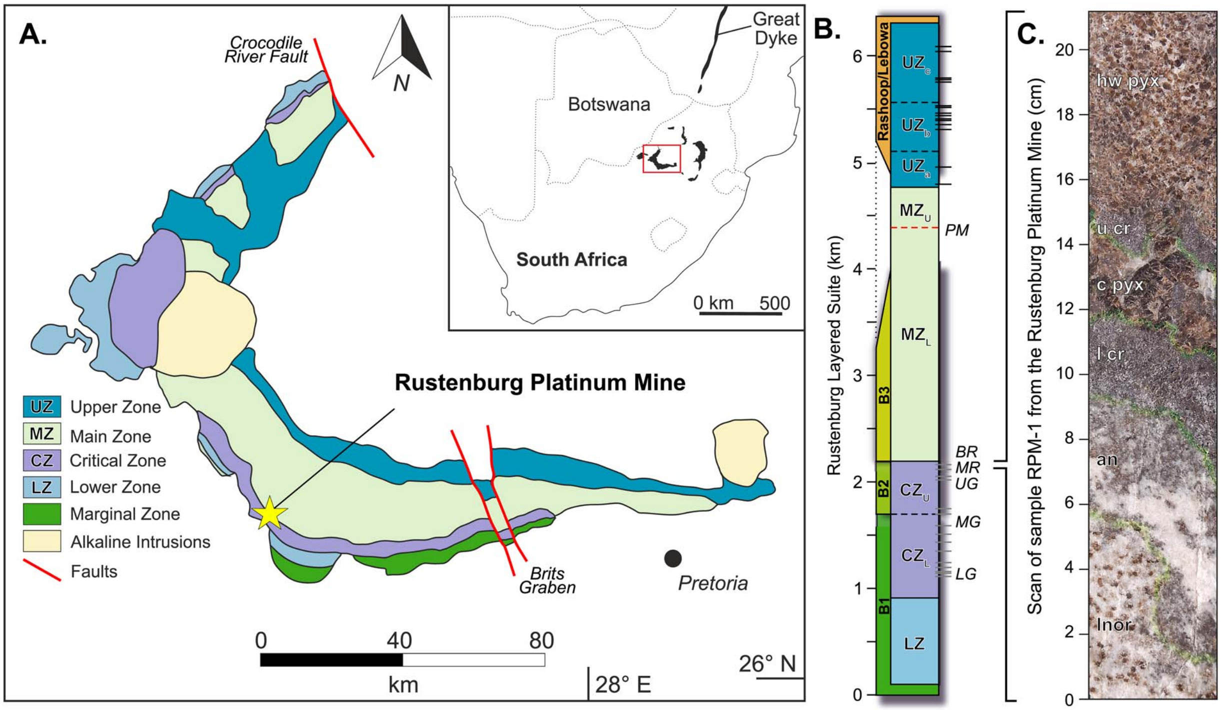

Fig. 1. Geological map (A) and schematic stratigraphic section (B) of the Bushveld Complex showing the location of the Rustenburg Platinum Mine in the western lobe (modified from Mungall *et al.* 2016). **C.** Annotated photograph of sample RPM-1 described in detail by Smith *et al.* (2021). Abbreviations: lnor = leuconorite, an = anorthosite, l cr = lower chromitite, c pyx = central pyroxenite, u cr = upper chromitite, hw pyx = hanging-wall pyroxenite.

In general, the Merensky Reef consists of a cm- to m-scale, coarse-grained to pegmatoidal pyroxenite (*i.e., central pyroxenite*) that is bracketed by mm-scale chromitite layers (*i.e.,* the lower and upper chromitites) and overlain by several metres of medium-grained pyroxenite, known as the *hanging-wall pyroxenite* (Viljoen *et al.* 1986b; Viljoen 1999; Barnes and Maier 2002; Arndt *et al.* 2005; Naldrett *et al.* 2009; Smith *et al.* 2021). In the western lobe of the Bushveld Complex, this sequence is typically underlain by leuconorite, anorthosite, and subordinate troctolite, whereas, in the eastern lobe, it is often underlain by pyroxenite (Eales and Cawthorn 1996; Barnes and Maier 2002; Roberts *et al.* 2007; Mitchell and Scoon 2007; Scoon and Costin 2018; Mitchell *et al.* 2019). Stratiform reef-style PGE mineralization manifests as PGE-rich disseminated sulfides and platinum-group minerals that are concentrated in the chromitites and central pyroxenite as well in the immediate footwall rocks (Viljoen and Hieber 1986; Barnes and Maier 2002; Mitchell and Scoon 2007; Naldrett *et al.* 2009; Mitchell *et al.* 2019; Smith *et al.* 2021; Barnes *et al.* 2022).

Several studies have concluded that the Merensky Reef directly overlies a regional unconformity and is related to a new injection of relatively primitive melt that erodes the resident cumulate pile (Irvine *et al.* 1983; Campbell 1986; Eales *et al.* 1988; Viljoen 1999; Viring and Cowell 1999; Roberts *et al.* 2007; Latypov *et al.* 2022). Some researchers have ascribed the formation of anorthosite and troctolite that underlies the Merensky Reef and various chromitites to the reconstitution of resident noritic cumulates during reaction with replenishing melt(s) (Eales *et al.* 1988; Viring and Cowell 1999; Roberts *et al.* 2007; Latypov *et al.* 2015; Maier and Barnes 2024). It has remained unclear as to whether such a process can explain the diversity of the Merensky footwall assemblages and contribute to the formation of stratiform PGE-bearing chromitites. In the present study, we use energy dispersive spectroscopy (EDS) element mapping, electron backscatter diffraction (EBSD), and mineral chemistry to characterize the floor rocks of so-called 'normal' Merensky Reef in the western lobe of the Bushveld Complex. These data are combined with thermodynamic simulations of footwall reconstitution using the Magma Chamber Simulator (Bohrson *et al.* 2014, 2020). It is argued that the footwall anorthosite, and possibly other footwall lithologies, form during the interaction between replenishing silicate melts and resident noritic cumulates.

GEOLOGICAL BACKGROUND

The Bushveld Complex in southern Africa has been described in numerous publications (Wager and Brown 1968; Eales and Cawthorn 1996; Maier *et al.* 2013; Cawthorn 2015; Kinnaird and McDonald 2018). The mafic-ultramafic layered rocks are grouped into the *Rustenburg Layered Suite*, which constitutes a ∼ 6-8 km package of cumulate rocks that host most of the world's PGE and Cr resources as well as significant Ni and Cu resources (Cawthorn 2015; Mudd *et al.* 2018). The *Rustenburg Layered Suite* is divided into five stratigraphic units, including the Marginal, Lower, Critical, Main, and Upper Zones (Fig. 1A-B). The majority of PGE, Cr, and V mineralization is present in the Critical Zone, which is commonly subdivided into a Lower Critical Zone consisting predominantly of orthopyroxenite with subordinate harzburgite and chromitite and an Upper Critical Zone consisting of interlayered norite, anorthosite, chromitite, and (ortho)pyroxenite (Cameron 1982).

The Merensky Reef occurs at the base of the so-called *Merensky Cyclic Unit* in the Upper Critical Zone (Fig. 1B). Although seemingly conformable at several localities, the basal contact of the Merensky Reef sequence may truncate several meters of underlying cumulates, suggesting that it shares a broadly unconformable contact with its footwall (Vermaak 1976; Viljoen and Hieber 1986; Viljoen 1999; Viring and Cowell 1999; Barnes and Maier 2002; Roberts *et al.* 2007; Mitchell and Scoon 2007; Latypov *et al.* 2015;

Mitchell *et al.* 2019). The presence of a magmatic unconformity is supported by the occurrence of elliptical structures (plan view) that transgress the floor rocks at a variety of scales (*dimples*, *potholes*, and *excursions*; Ballhaus 1988; Carr *et al.* 1999; Viring and Cowell 1999; Smith and Basson 2006). At localities where potholes and undercuttings are present, the Merensky Reef may be referred to as '*potholed*' reef (Buntin *et al.* 1985; Ballhaus 1988; Viljoen 1999; Carr *et al.* 1999; Roberts *et al.* 2007; Latypov *et al.* 2015, 2017). In the western lobe, regional variation in the nature of the Merensky Reef led to its division into Swartklip and Rustenburg (*cf.* Kroondal facies of Wagner 1929) facies to the north and south of the Pilanesberg Complex, respectively (Wagner 1929; Viljoen 1999). In Swartklip facies, the stratigraphic thickness between the Merensky Reef and UG2 is markedly attenuated and comprises a far greater relative proportion of olivine-bearing lithologies as well as a PGE-bearing Psuedo Reef package (Viljoen 1999; Mitchell *et al.* 2019). At Northam (Swartklip facies), the Merensky Reef has been subdivided into *normal* and *potholed* reef, the latter being underlain by olivine norite and troctolite (Smith *et al.* 2004; Roberts *et al.* 2007). The Merensky Reef in the Rustenburg facies is also subdivided into four subfacies; three of which are narrow, pegmatoidal Merensky Reef overlying anorthosite that display variations in lithological thickness and the degree of potholing, and the fourth is named non-pegmatoidal wide reef subfacies (Viljoen 1999). Within the three narrow pegmatoidal Merensky Reef subfacies occurs a *normal* narrow (< 20) reef overlying anorthosite, referred to as *thin reef facies* in Wilson (1999). This is the subject of the present contribution.

In the Rustenburg facies, *normal* Merensky Reef refers to the regionally traceable and planar portions of the reef stratigraphy that still unconformably overly the footwall lithologies but that record relative uniformity in thickness and nature. In general, apparently conformable relationships persist at sites of consolidated melanocratic floor rocks, whereas unconformable relationships predominantly occur at sites of leucocratic floor rocks (Viring and Cowell 1999). In the western lobe, leuconorite and anorthosite are the lithologies that most often underlie the Merensky Reef (Leeb du Toit 1986, Viljoen and Hieber 1986; Maier and Eales 1997). An mm- to dm-scale layer of anorthosite often separates the leuconorite from the lower chromitite, and a μm- to mm-scale layer of "pure" anorthosite (known as the "bleached zone") directly underlies the lower chromitite (Nicholson and Mathez 1991; Smith *et al.* 2021). The thickness of this anorthosite "bleached zone" apparently positively correlates with the thickness of the lower chromite (Nicholson and Mathez 1991). In parts of the western lobe (*e.g.,* Turfspruit and Wolhunterskop), the anorthosite may be mottled (*i.e.,* containing large oikocrysts of olivine and pyroxene) or spotted (*i.e.,* containing equant pyroxene crystals interpreted to be of cumulus origin) (Maier and Eales 1997). In the eastern limb (*e.g.,* Winnaarshoek and Atok), the Merensky Reef sequence is hosted amongst layered norite, gabbronorite, and feldspathic orthopyroxenite (Cameron 1970; Lee and Butcher 1990; Mathez *et al.* 1997; Mitchell and Scoon 2007).

This study is concerned with normal (relatively thin) Merensky Reef sampled at the Rustenburg Section of the Rustenburg Platinum Mines (Fig. 1C; Viljoen and Hieber 1986; Nicholson and Mathez 1991; Wilson *et al.* 1999; Smith *et al.* 2021). At this location, the central pyroxenite is coarse-grained and ranges from a few cm to up to 1 m in thickness (Viljoen and Hieber 1986; Wilson *et al.* 1999). This unit is bracketed by two mm-scale chromitite layers. The upper chromitite is discontinuous and compacted relative to the lower chromitite. The lower chromitite is underlain by a cm- to dm-scale layer of anorthosite, which in turn, is underlain by barren leuconorite (Wilson *et al.* 1999; Smith *et al.* 2021). The upper chromitite is overlain by a medium-grained hanging-wall pyroxenite. Disseminated sulfides are prevalent in the central pyroxenite and chromitites, and they further extend downwards into the immediate anorthosite footwall as well as concentrate in the lowermost portion of the hanging-wall pyroxenite (*i.e.,* directly above the upper chromitite).

MATERIALS AND METHODS

This study performs microtextural analyses on sections produced from a 30 x 10 x 2 cm sample (RPM-1) of the Merensky Reef from the Rustenburg Platinum Mine (Fig. 1C) (Smith *et al.* 2021). Methods are detailed in Electronic Supplementary Material (ESM) 1. Data and a summary of thermodynamic forward models are given in ESM 2. Raw data files and model outputs can be accessed from the digital data archive at doi.org/10.25919/rgb7-ch54.

Both EDS and EBSD maps were produced at Cardiff University using a Zeiss Sigma HD Analytical Field Emission Gun Scanning Electron Microscope equipped with two Oxford Instruments 150 mm^2 energy dispersive spectrometers and a Nordlys EBSD detector inserted to 191 mm. The data were subsequently processed using MTEX (Bachmann *et al.* 2010) and the J-, M-, L#, and F# indices have been used to evaluate mineral fabrics, which were calculated on their respective orientation density function (ODF) (Bunge 1982; Skemer *et al.* 2005; Mainprice *et al.* 2015; Cheadle and Gee 2017). The ODFs were calculated using a de la Valée Pousin kernel with a half-width of 10°. Crystal size distribution (CSD) profiles of chromite were determined using CSDCorrections v1.6 (Higgins 2000).

The compositions of silicates (Table 1 and ESM 2) were determined at Camborne School of Mines (University of Exeter) using a JEOL JXA-8200 electron-probe microanalyzer over four analytical sessions (ESM 2; doi.org/10.25919/rgb7-ch54). Detection limits for Ca, Mg, and K were below 200 ppm, those for Al, Na, Mn, and P were below 400 ppm, those for Al and Mn were below 150 ppm, and those for Si, Fe, Cr, and Ti were below 600 ppm. An EPMA map of chromite crystals in the lower chromitite was produced using a Cameca SX-Five EPMA at the Centre de Microcaractérisation Raimond Castaing (University Paul Sabatier, Toulouse).

Chromite compositions (ESM 2) were determined by LA-ICP-MS at LabMaTer, Université du Quebec, using an Excimer 193 nm resolution M-50 LA system (Australian Scientific Instrument) equipped with a double volume cell S-155 (Laurin Technic) and coupled with an Agilent 8900 mass spectrometer. The tuning parameters were a laser frequency of 15 Hz, a power of 3 mJ/pulse, a dwell time of 7.5 ms, and a fluence of 5 J/cm^2. The beam size was 44 μm and line scans were carried out across the grains with a stage speed of 10 μm/s. The ablated material was carried into the ICP-MS by an Ar–He gas mix at a rate of 0.8–1 L/min for Ar and 350 mL/min for He, and 2mL/min of nitrogen was also added to the mixture. Data reduction was carried out using the Iolite package for Igor Pro software (Paton et al. 2011). External calibration was carried out GSE-1g and NIST-610 (supplied by USGS) and results were monitored using GProbe 6, a basaltic glass, and natural chromite crystals from in-house reference materials (G-12 G seam Stillwater Complex and BC-16 massive chromite UG2). The results obtained for the monitors agree within analytical error with the working values (ESM 2), except for Sc in NIST-616 due to interference from Si. Mineral formulae were recalculated using GCDKit.Mineral (Janoušek *et al.* 2024).

Table 1: Summary of silicate mineral compositions.

Phase:	**Orthopyroxene**												**Clinopyroxene**			
Rock type:	leuconorite				lnor-an transition				Lower chromitite				anorthosite			
Grain type:	Oikocryst				Oikocryst				Oikocryst				Oikocryst			
# Grains:	29 spots & 4 transects				5 spots & 3 transects				3 spots				5 spots			
Statistic:	*min*	*max*	*ave*	2σ	*min*	*max*	*ave*	2σ	*min*	*max*	*ave*	2σ	*min*	*max*	*ave*	2σ
SiO_2	53.2	57.4	56.3	2.35	53.2	56.5	55.4	1.96	55.4	57.2	56.5	1.02	52.7	53.7	53.3	0.69
TiO_2	0.11	0.28	0.18	0.09	0.11	0.36	0.23	0.18	0.06	0.35	0.16	0.16	0.48	0.56	0.52	0.07
Al_2O_3	1.14	2.92	1.55	0.82	0.88	2.53	1.57	0.94	0.56	2.28	1.51	0.78	1.69	2.1	1.89	0.31
Cr_2O_3	0.35	0.59	0.50	0.11	0.24	0.56	0.46	0.20	0.24	0.55	0.45	0.15	0.72	0.93	0.81	0.15
FeO	12.8	14.0	13.4	0.58	13.4	16.1	14.5	1.74	11.7	13.2	12.8	0.84	5.3	6.1	5.66	0.61
MnO	0.21	0.30	0.26	0.04	0.24	0.33	0.27	0.06	0.09	0.31	0.24	0.10	0.13	0.18	0.16	0.04
MgO	28.4	29.7	28.9	0.55	27.6	28.8	28.2	0.76	28.4	30.4	29.3	1.14	16.0	16.3	16.1	0.24
CaO	0.92	2.09	1.66	0.62	0.99	2.35	1.52	0.79	0.36	2.14	1.31	1.22	22	23.0	22.8	0.46
Mg#	78.6	80.0	79.3	0.77	75.5	79.2	77.6	2.32	79.5	82.3	80.4	1.54	82.6	84.5	83.6	1.43
En	75.8	77.8	76.8	0.99	74.1	76.8	75.3	1.98	76.2	79.9	78.3	2.34	44.9	45.5	45.2	0.49
Fs	19.4	20.8	20.0	0.87	20.2	24.0	21.8	2.45	17.2	20.0	19.1	1.57	8.32	9.56	8.90	0.92
Wo	1.75	4.05	3.19	1.23	1.91	4.54	2.93	1.55	0.70	4.09	2.51	2.29	45.0	46.3	45.9	1.06

Phase:	**Plagioclase**											
Grain type:	Cumulus				Cumulus				Oikocryst			
Rock type:	leuconorite				anorthosite				Lower chromitite			
# Grains:	4 transects				4 transects				1 transect			
Statistic:	*min*	*max*	*ave*	2σ	*min*	*max*	*ave*	2σ	*min*	*max*	*ave*	2σ
SiO_2	45.1	54.1	50.0	1.87	46.7	66.0	50.5	2.16	47.0	51.7	50.5	1.88
Al_2O_3	27.6	32.0	30.9	1.43	20.0	32.2	30.9	1.82	30.2	33.4	31.0	1.26
CaO	11.6	16.4	15.1	1.54	2.44	16.9	15.3	2.16	13.9	18.2	15.1	1.55
Na_2O	1.89	4.73	2.81	0.64	2.19	10.7	2.91	1.03	1.39	3.47	3.04	0.80
K_2O	0.11	0.76	0.19	0.15	0.03	1.30	0.18	0.17	0.03	0.69	0.15	0.14
FeO	0.19	3.17	0.38	0.80	0.05	5.19	0.44	0.85	0.14	0.65	0.25	0.17
An	57.5	80.1	74.8	5.63	11.9	81.0	74.3	9.78	69.4	87.8	73.2	7.08

[1] Mg# = 100 x Mg/[Mg + Fe] mol.%, En = 100 x Mg/[Mg+Fe+Ca] mol.%, Fs = 100 x Fe/[Mg+Fe+Ca] mol.%, Wo = 100 x Ca/[Mg+Fe+Ca] mol.%, An = 100 x Ca/[Ca+2Na] mol.%

RESULTS

Footwall leuconorite

The leuconorite contains ~ 25-30% orthopyroxene, ~ 60-70% plagioclase and traces of intercumulus clinopyroxene (~ 1-3%) and quartz (~ 0.5-1%). Orthopyroxene crystals (~ 1-5 mm in diameter) are anhedral and possess thin (< 1 mm) poikilitic overgrowths that are often partially surrounded by intercumulus clinopyroxene (Fig. 2A-B). Accessory chromite crystals occur at the margins of orthopyroxene oikocrysts throughout the leuconorite, relatively increasing at the leuconorite-anorthosite contact as well as in proximity to intercumulus clinopyroxene (ESM 3i), before virtually vanishing above the leuconorite-anorthosite contact. Accessory phlogopite, apatite, and Fe-Ti oxides occur throughout the feldspathic domains. Sulfide blebs (pyrrhotite-pentlandite-chalcopyrite) with interstitial morphologies are also most abundant in the uppermost part of the unit, where they are spatially associated with intercumulus quartz and pyroxenes as well as complexly zoned cumulus plagioclase. The orthopyroxene crystals have 80.0-78.6 mol.% Mg#, 0.59-0.35 wt.% Cr_2O_3, and display normal compositional zoning whereby Cr_2O_3 values decrease from core to rim while TiO_2 concentrations increase (Fig. 3A-B; ESM 2). Cumulus plagioclase crystals (~ 1 mm of equivalent radius) are subhedral and have An contents ranging from 78.1-71.5 mol.%. They display no systematic compositional zonation in the studied sections (Fig. 3C).

Fabrics for plagioclase and orthopyroxene are not random (Fig. 2C-D). For both phases, the [010] axes are oriented normal to the compositional layering, while the [100] and [001] axes form a girdle on the layering plane. The fabric recorded by cumulus plagioclase is relatively weak (J-index = 1.79), yet comparable to magmatic fabrics recorded by the gravitational settling of cumulus tabular phases (Satsukawa *et al.* 2013; Holness *et al.* 2017; Cheadle and Gee 2017). The fabric recorded by orthopyroxene crystals is relatively stronger (J-index = 5.30), though it is likely biased because of the few orthopyroxene crystals sampled as well as their poikilitic nature.

For all phases, only rare indicators of plastic deformation exist, such as sub-grains in orthopyroxene and plagioclase (Fig. 2E-G). Cumulus plagioclase crystals are extensively twinned with straight twin boundaries that crosscut the entire crystals. The EBSD data indicate that the Albite, Carlsbad-A and Albite-Carlsbad-A twin laws make up most of the twin interfaces in the footwall norite. Investigation of the relationship between orthopyroxene crystals and their associated interstitial clinopyroxene rims revealed a non-random and consistent distribution of their crystallographic axis; orthopyroxene [100], [010], and [001] parallels clinopyroxene [100], [010], and [001], respectively (ESM 3ii). This parallel relationship between the two pyroxenes suggests that clinopyroxene is using previously existing orthopyroxene as a crystallization substrate (ESM 3ii).

In the upper ~ 1 cm of the leuconorite (*i.e.,* at the contact with the anorthosite), the relative width of poikilitic orthopyroxene rims increase (ESM 3iii), and cumulus plagioclase crystals display more complex oscillatory zoning, albeit with An contents (77.1-72.7 mol.%) similar to those analyzed in the underlying leuconorite (Figs. 3C). On average, orthopyroxene crystals here have lower Mg# values (79.2-75.5 mol.%) and similar Cr_2O_3 (0.56-0.24 wt.%) concentrations relative to those analyzed in the underlying leuconorite (Fig. 3A-B).

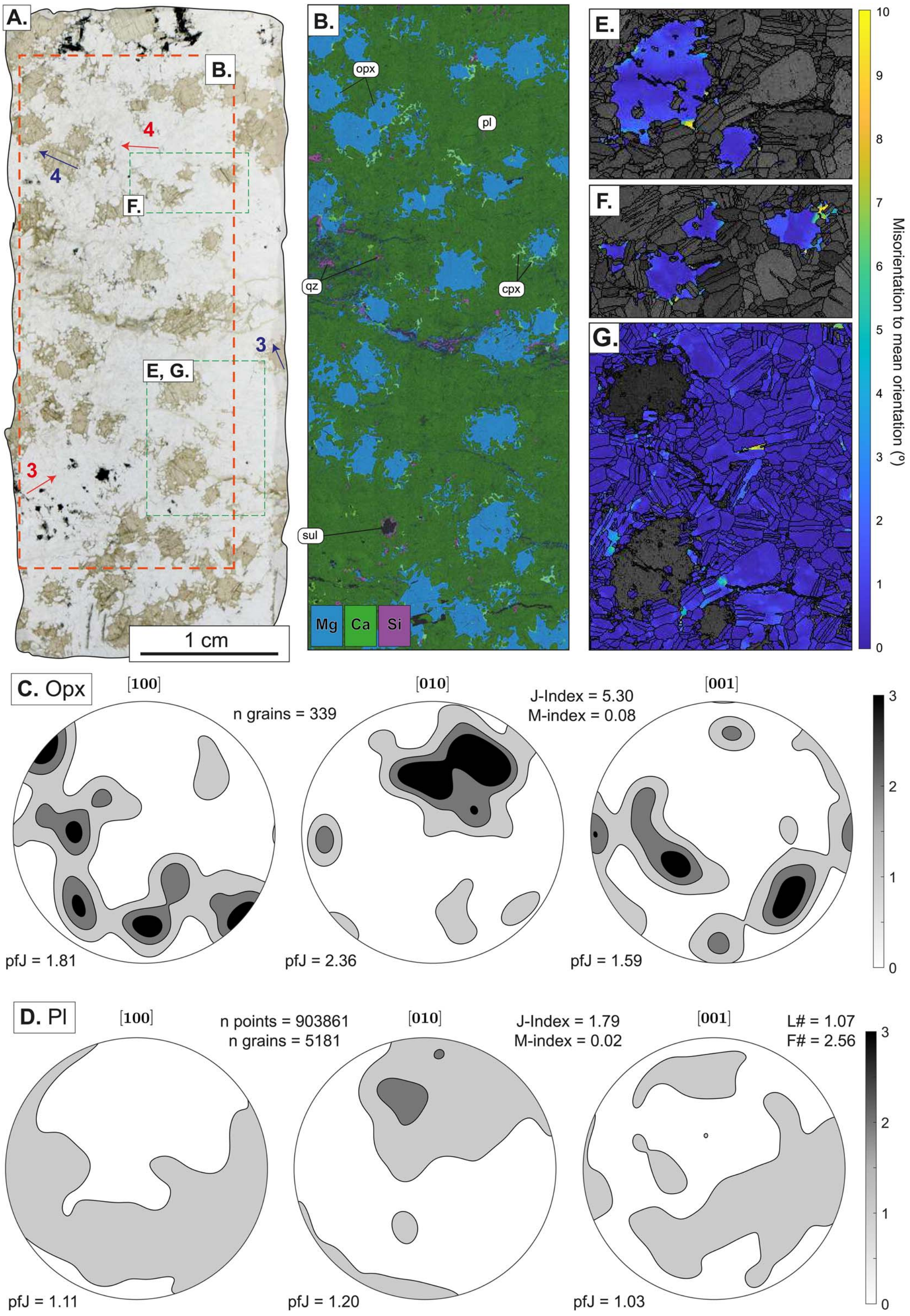

Fig. 2. Summary of map data acquired for the leuconorite. **A.** Scanned image of section B1 showing analyzed areas and locations of EPMA profiles in orthopyroxene (blue arrows) and plagioclase (red arrows). **B.** Mg-Ca-Si element map displaying cumulus plagioclase (pl), orthopyroxene (opx) with intercumulus outer margins, as well as traces of intercumulus clinopyroxene (cpx) and quartz (qz). **C.** Lower hemisphere, equal-area pole figures of the [100], [010], and [001] axes of orthopyroxene crystals (one point per crystal). **D.** Lower hemisphere, equal-area pole figures of the [100], [010], and [001] axes of all measurements from plagioclase crystals. **E-F.** Map of misorientation-to-mean orientation of orthopyroxene crystals. Note the small amounts of misorientation confined to the rims. **G.** Map of misorientation-to-mean orientation of cumulus plagioclase crystals showing minimal evidence of deformation.

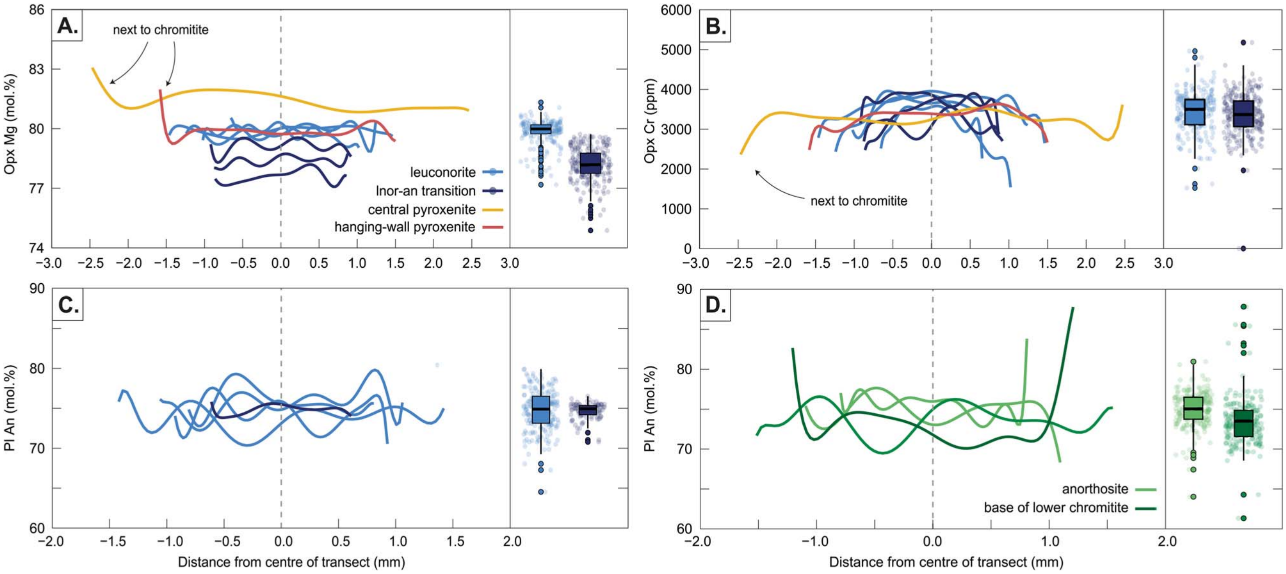

Fig. 3. A-B. Rim-core-rim transects of Mg# (mol.%) and Cr (ppm) contents of orthopyroxene crystals analyzed in the leuconorite together with an orthopyroxene crystal analyzed in the central and hanging-wall pyroxenites (blue transects 8 and 9 in Fig. 6). Orthopyroxene crystals at the leuconorite-anorthosite (lnor-an) transition have lower Mg# values and similar Cr concentrations compared with those from the underlying leuconorite. The Mg# values are broadly flat, whereas Cr concentrations decrease towards crystal rims. Note that the orthopyroxene crystal from the central pyroxenite has higher Mg# values, which increase with proximity to chromite crystals. **C-D.** Transects of An contents for plagioclase crystals in the footwall anorthosite and at the base of the lower chromitite. Plagioclase crystals show no discernible systematic zoning. The crystal analyzed in the lower chromitite shows pronounced reverse zoning, though this does not represent rim-core-rim but a portion of a plagioclase oikocryst that occupies the space between two chromite crystals (red transect 9 in Fig. 6). Box-and-whisker diagrams with jittered data points are included and the lines represent polynomial approximations.

Footwall anorthosite

The anorthosite (∼ 3-4 cm thick) forms the immediate footwall to the reef with which it shares a knife-sharp contact. Its contact with the leuconorite is fairly sharp and marked by an abrupt decrease in the modal abundance of orthopyroxene (*e.g.,* from 25 to 0.5%). Approximately 95% of the unit consists of subhedral cumulus plagioclase (up to ∼ 3 mm in length) that possess An contents of 78.7-63.8 mol.% and complex oscillatory zoning (Figs. 3D, 4A-B). Chromite, apatite, and Fe-Ti oxides are accessory phases. Sulfides (∼ 1-2%) occur within sub-vertical domains, together with quartz, pyroxenes, and phlogopite, that traverse the entire anorthosite and gradually dissipate at the leuconorite-anorthosite contact. The sulfides consist of fairly equal proportions of pentlandite, chalcopyrite, and pentlandite.

Microstructurally, the anorthosite is similar to the leuconorite. The cumulus plagioclase crystals are subhedral, with long axes that are often parallel to the compositional layering. The crystals record a weak but non-random fabric with [010] axes that cluster normally to the layering plane as well as a well-defined girdle for the [100] axes on the layering plane (J-index = 2.47) (Fig. 4C). Cumulus plagioclase crystals display limited evidence for internal deformation and similar twin laws to those analyzed in the leuconorite (Fig. 5A-C).

Beginning approximately 1 cm beneath the lower chromitite, is a ∼ 5-mm-thick layer of anorthosite that contains clinopyroxene oikocrysts ($Mg\#_{82.6-84.5}$; mode ∼ 8-10% of this interval) and interstitial orthopyroxene (∼ mode 3-5% of this interval) as well as accessory quartz and phlogopite (< 1%; Fig. 5A). The clinopyroxene oikocrysts record variable degrees of internal misorientation (Fig. 5D-E) that is consistent with either limited plastic deformation during late-stage compaction or the growth of complexly-shaped oikocrysts with large lateral extents. The uppermost 5 mm of this unit (*i.e.,* directly below the *lower chromitite*) is an almost pure seam of anorthosite (*bleached zone* of Nicholson and Mathez (1991)), containing coarse-grained plagioclase crystals (up to ∼ 8 mm in length) that extend from the anorthosite into the lower chromitite. Cumulus plagioclase in these uppermost portions possess [010] axes normal to the layering plane and [100] axes scattered in a girdle on the layering plane (J-index = 4.66; Fig. 5F). The fabric indices for this uppermost portion are stronger than those recorded in the underlying lithologies.

Lower chromitite and central pyroxenite

The lower chromitite is approximately 1.5 to 3 cm thick and shares a knife-sharp contact with the underlying anorthosite. The unit consists of ∼ 50% chromite, where crystals manifest as: (i) relatively coarser amoeboidal crystals that commonly display hook-like features (ESM 3iv; *cf.* Yudovskaya *et al.* 2019) and enclose polymineralic silicate or sulfide inclusions; and (ii) relatively finer blocky subhedral crystals that are devoid of inclusions and commonly clustered (see also Li *et al.* 2005; Vukmanovic *et al.* 2013). The chromite crystals are hosted by plagioclase oikocrysts (∼ 30-35%) in the lower two-thirds of the unit and by orthopyroxene oikocrysts (∼ 20-25%) in the upper third of the unit (Fig. 5A). Rutile is a common accessory phase in the upper orthopyroxene-hosted portion of the chromitite, whereas accessory phlogopite, apatite, clinopyroxene, and sulfides occur throughout the chromitite (Fig. 6A-B). Thick section D1 samples the lower portion of the central pyroxenite, which consists mostly of coarse-grained orthopyroxene (∼ 80-90%) with accessory plagioclase (∼ 1-4%; An_{68-64}), clinopyroxene (∼ 2-5%), chromite (∼ 2-4%), quartz, phlogopite, and sulfides.

One plagioclase crystal sampled towards the base of the lower chromitite is strongly reversely zoned (Fig. 3D); the areas directly adjacent to chromite are 10 mol.% more anorthitic than the remaining transect (see also Smith *et al.* 2021). Orthopyroxene

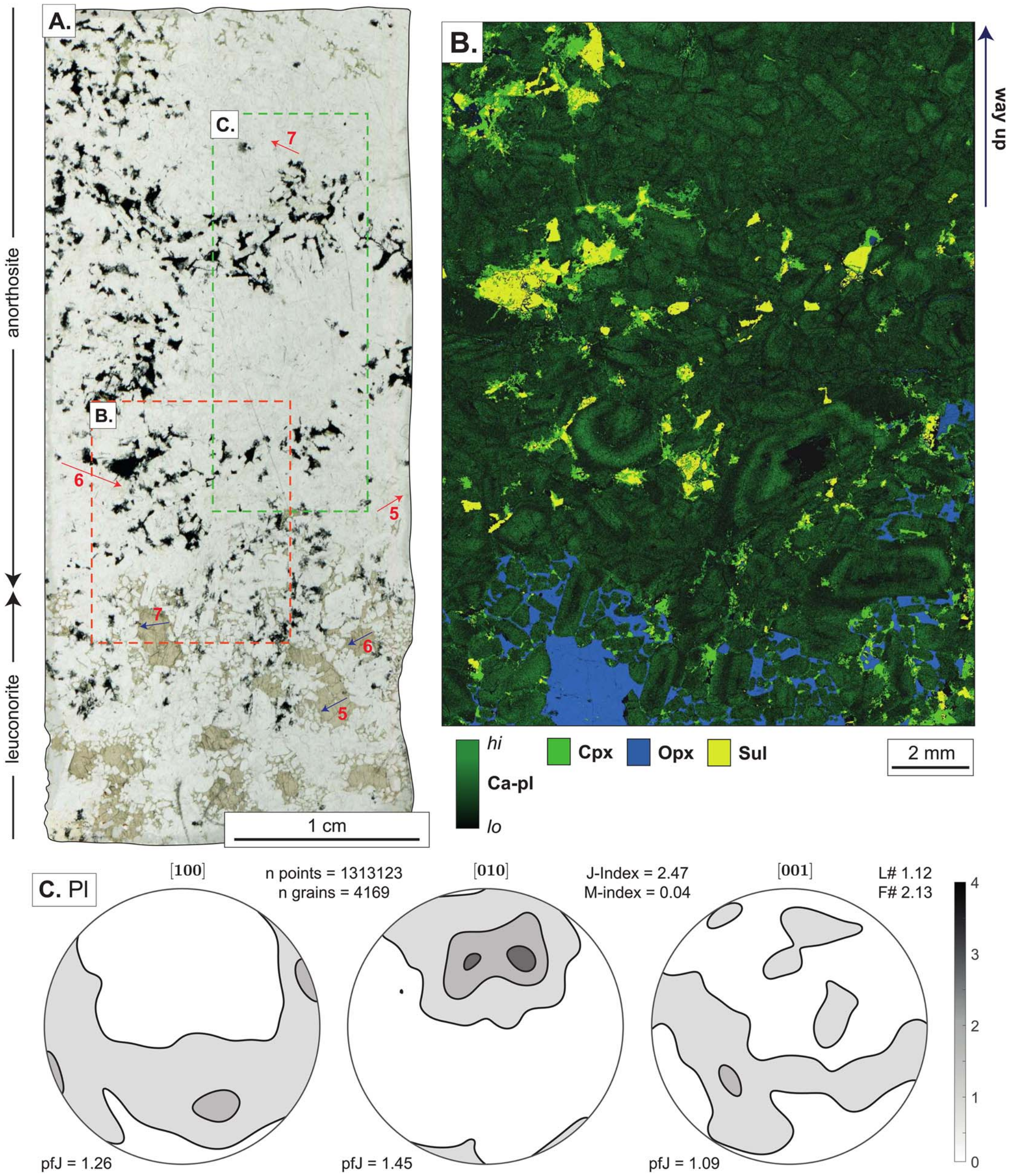

Fig. 4. Summary of map data acquired for the lower portion of the footwall anorthosite. **A.** Scanned image of section C1 showing the analyzed areas (blue arrows for orthopyroxene, red arrows for plagioclase). **B.** Ca-Na element map highlighting complex plagioclase zoning at the leuconorite-anorthosite contact. **C.** Lower hemisphere, equal-area pole figures of the [100], [010], and [001] axes of all measurements taken on plagioclase crystals.

in the chromitite and pyroxenite are relatively less evolved ($Mg_{\sim 84}$) than those analyzed in the footwall, yet with similar Cr_2O_3 and TiO_2 concentrations. Orthopyroxene analyses proximal to chromite crystals (< 2 mm) have relatively higher Mg_{opx} as well as lower Cr and Ti concentrations (Fig. 3A-B). In contrast to underlying cumulus plagioclase, plagioclase oikocrysts appear to be orientated with their (010) planes normal to the layering plane and with their a- [100] and c-axis [001] being scattered on the vertical plane, while orthopyroxene oikocrysts have their (010) planes coincident to the layering plane. Internal misorientation is observed within the plagioclase oikocrysts, beginning at the anorthosite-chromitite contact. The orthopyroxene oikocryst within the chromitite shows some internal misorientation, yet there is little evidence of internal deformation in the orthopyroxene in the uppermost portion of the chromitite.

Regardless of their stratigraphic level and host phase, blocky chromite crystals show no signs of lattice bending (Fig. 6C-D). Conversely, amoeboidal chromite crystals can either be free of lattice misorientation or show evidence of extensive lattice bending, where the latter may resemble subgrains or undulose extinction as observed in non-isotropic minerals. No common structures for the subgrains were apparent in the amoeboidal chromite. The greatest degree of lattice bending is observed in crystals that display the most complex and concave crystal boundaries. Amoeboidal crystals generally have relatively larger equivalent radii (> 0.2 mm) and crystal orientation spread values (> 1°), making them somewhat distinguishable from blocky grains. The CSD profile for all lower chromitite crystals is concave at crystal sizes < 0.16 mm and displays a well-defined kink at crystal sizes of ~ 0.38 mm. Crystals with sizes below 0.38 mm (0.10-0.38 mm)

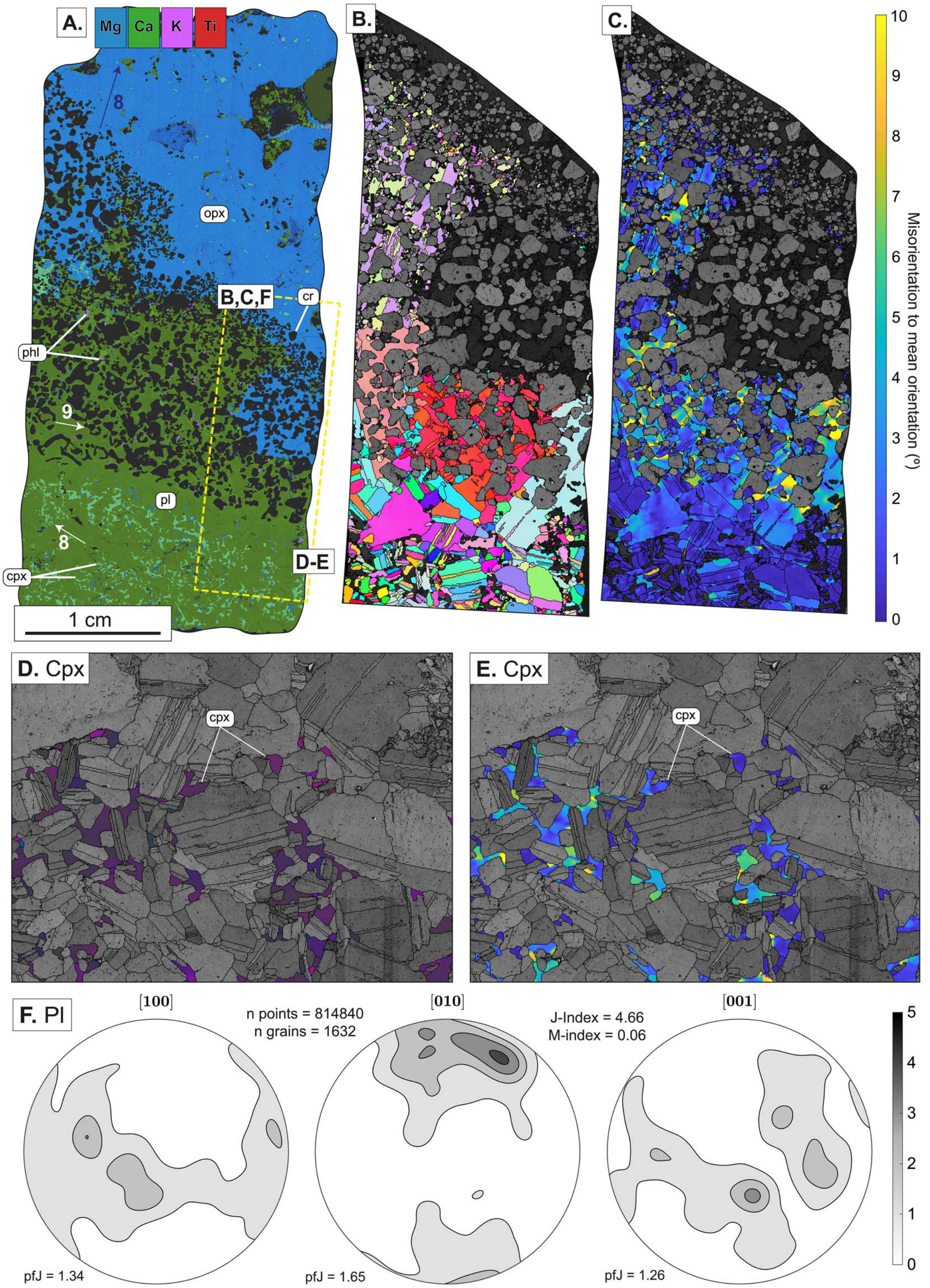

Fig. 5. Summary of data acquired for the upper portion of the footwall anorthosite. **A.** Mg-Ca-Si element map of section D1 displaying textures at the anorthosite-lower chromitite-central pyroxenite interval. Note that the upper portion of the anorthosite is essentially leucogabbro with the exception of a nearly pure layer of anorthosite directly beneath the lower chromitite. **B-C.** Mean orientation (similar colors mean similar orientations) and misorientation-to-mean orientation maps of plagioclase. Note the large plagioclase oikocrysts are orientated with their (010) planes normal to the layering plane and display large degrees of localized misorientation. **D-E.** Mean orientation and misorientation-to-mean orientation maps of a clinopyroxene oikocryst in the anorthosite beneath the lower chromitite. **F.** Lower hemisphere, equal-area pole figures of the [100], [010], and [001] axes of all measurements taken on plagioclase crystals.

are defined as y = -14.3x + 7.5 (r^2 = 0.989) and crystals with sizes above 0.38 mm kink (0.38-1.21 mm) are defined as y = -6.3x + 4.6 (r^2 = 0.999) (Fig. 6E-F). The concave profile at small crystal sizes is predominantly defined by plagioclase-hosted crystals, while the kink is best displayed in orthopyroxene-hosted crystals.

Semi-quantitative EDS element maps show that chromite Cr# and Ti contents increase upwards through the lower chromitite, while Mg# values decrease upwards (Fig 7A-C). More specifically, it appears that chromite crystals hosted by, or proximal to, orthopyroxene have relatively higher Cr# and lower Mg# contents.

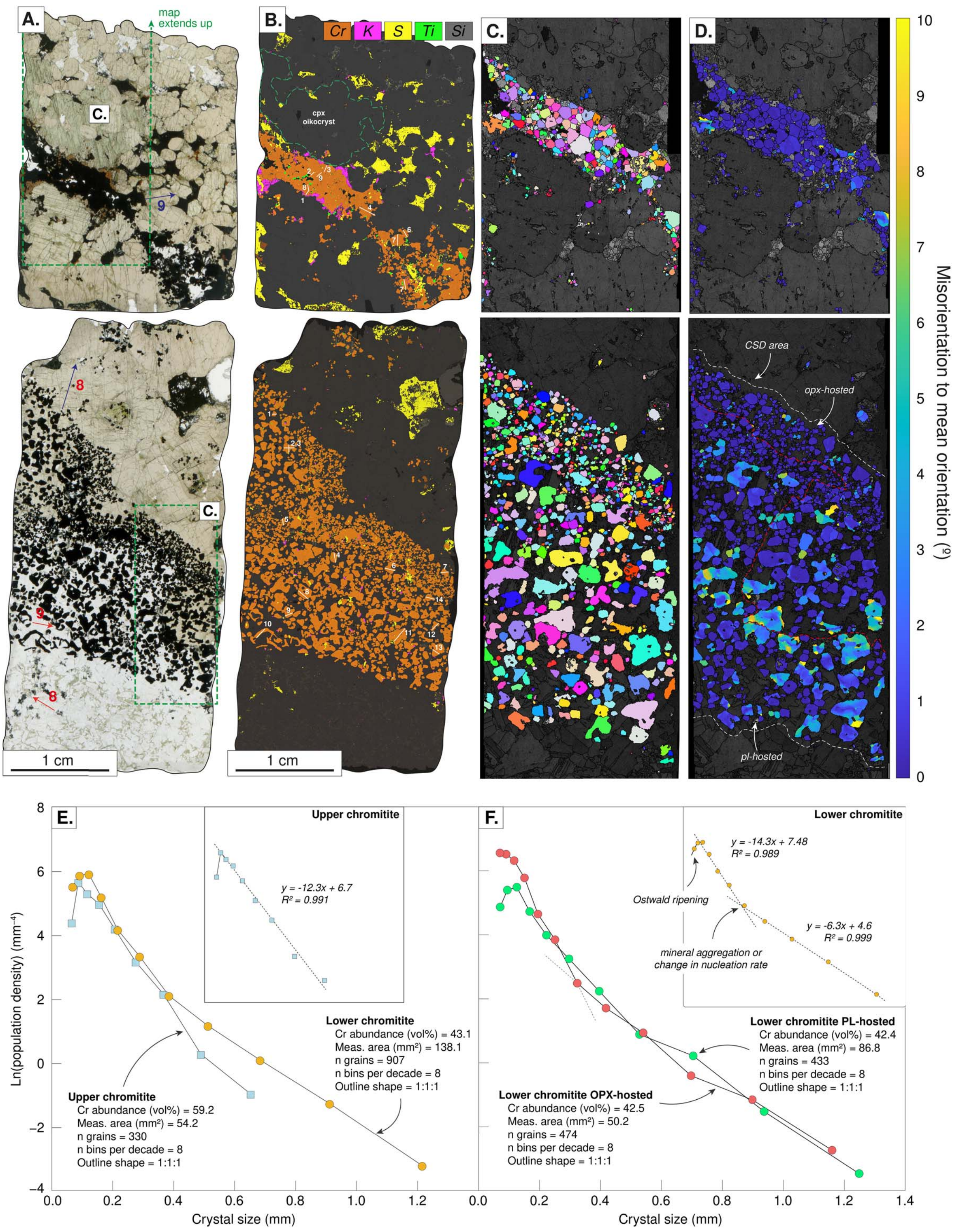

Fig. 6. Microtextural data acquired for the lower and upper chromitites. **A.** Plane-polarized light scans of sections D1 and E1, showing the locations of analyses. **B.** Cr-K-S-Ti-Si element map highlighting the distribution of sulfides, rutile, and phlogopite (white lines are chromite LA-ICP-MS transects). **C-D.** Mean orientation and misorientation-to mean orientation maps of chromite. Note the seemingly random distribution of chromite grains, which themselves occur as either: (i) relatively coarse and amoeboidal crystals with large degrees of misorientation; (ii) relatively fine and blocky crystals with no internal misorientation. **E-F.** Crystal size distribution curves for chromite crystals. Each profile displays concave patterns at crystal sizes < 0.2 mm and shallow convex patterns at crystal sizes > 2 mm. Note the 'kink' at ~ 0.34 mm in the profiles of orthopyroxene-hosted crystals in the lower chromitite.

However, this is not always the case and would need to be examined in three dimensions. A high-resolution EPMA element map (Fig. 7D) shows that there are no obvious chemical differences between amoeboidal and blocky crystals and it appears that the portion of mapped amoeboidal crystal submerged by orthopyroxene has relatively higher TiO_2 and Fe_2O_3 contents, as well as relatively lower Cr_2O_3 contents. There is no discernible chemical gradation in the plagioclase-hosted amoeboidal crystal.

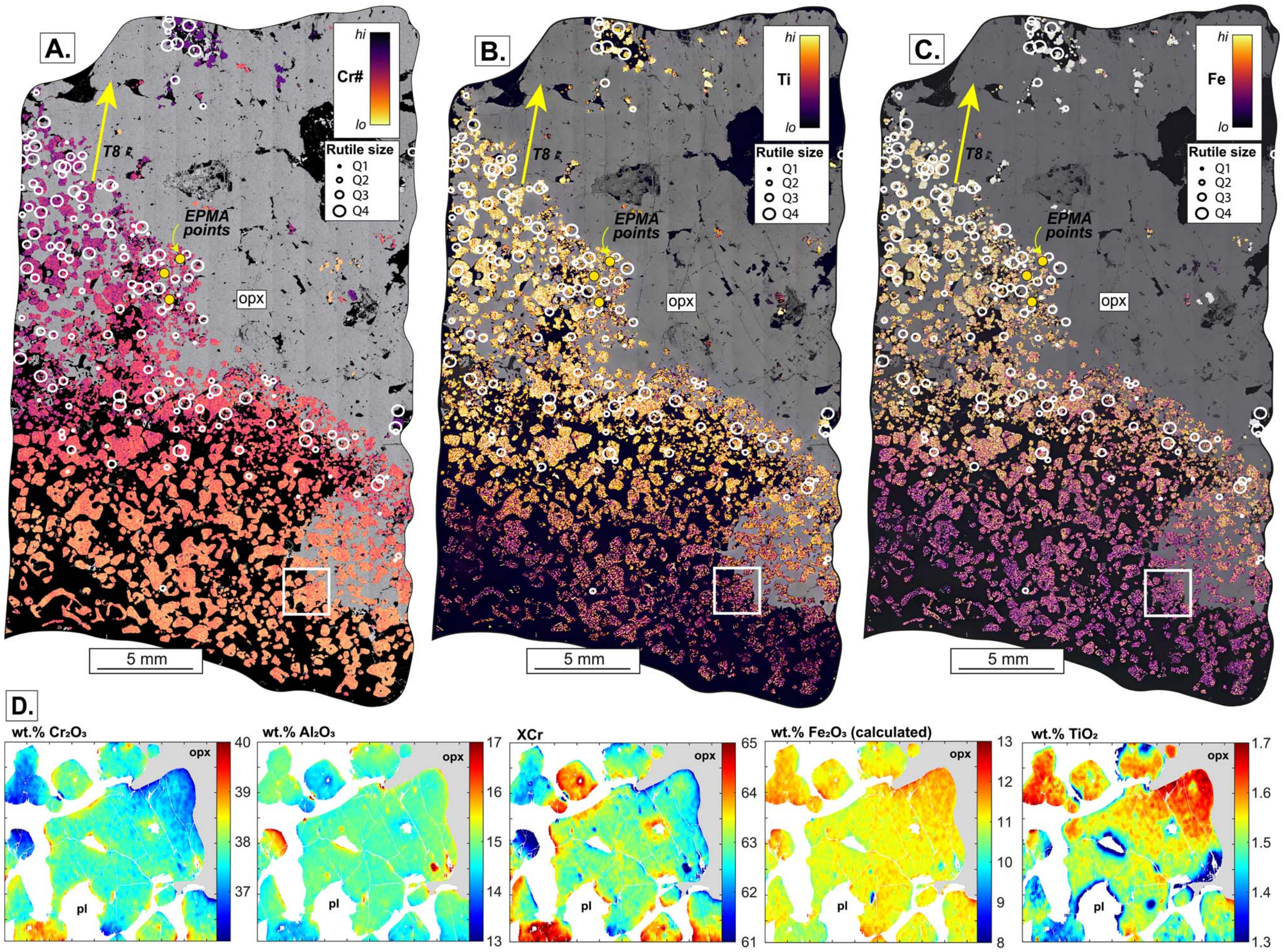

Fig. 7. Chemical maps of chromite crystals in the lower chromitite. **A-C.** Semi-quantitative EDS maps of Cr# values, Ti concentrations, and Fe concentrations. The grey phase is orthopyroxene (opx) and all other phases are in black. White circles indicate rutile and yellow annotations are the locations of EPMA analyses. Note that chromite crystals in the upper portion of the lower chromitite are relatively Al-poor, Ti-rich, and Fe-rich, and also coincide with the appearance of accessory rutile. **D.** EPMA map of chromite crystals occurring at the contact between plagioclase and orthopyroxene oikocrysts. Although there appears to be compositional change with proximity to orthopyroxene, this pattern does not extend to all orthopyroxene-hosted crystals.

There is negligible inter- and intra-grain chemical variation in lower chromitite crystals, including between amoeboidal and blocky subtypes (Table 2; Fig. 8). The chromite crystals have 29.6-34.7 mol.% Mg#, 64.8-70.3 mol.% Cr#, and 1.3-2.6 wt.% TiO_2. In general, Mg# contents decrease with increasing Cr# contents; plagioclase-hosted crystals have higher Mg# and lower Cr# contents, whereas orthopyroxene-hosted crystals in the uppermost portion have lower Mg# and higher Cr# contents. Chromite crystals in the latter group have compositions that are somewhat intermediary between lower and upper chromitite crystals. Vanadium and Mn concentrations increase with decreasing Mg# contents, whereas Sc and Ga decrease with decreasing Mg# contents.

Upper chromitite and base of the hanging-wall pyroxenite

The upper chromitite is much thinner (< 0.5 cm), more equilibrated, and less continuous relative to the lower chromitite (Fig. 6A-B). Our section samples the upper chromitite in two parts that have relatively different appearances. The portion underlying a large clinopyroxene oikocryst possesses highly compacted blocky chromite grains with negligible amounts of interstitial silicates that collectively are bound by orthopyroxene and phlogopite (Fig. 6B). The other portion comprises weakly compacted chromite grains (~ 55-60%) associated with plagioclase oikocrysts (~ 12-15%) as well as intercumulus clinopyroxene (~ 2-3%), quartz (~2-4%), phlogopite (< 1%), and rutile (~2-3%). Sulfides are disseminated throughout this unit (~ 4-5%).

Chromite crystals are generally blocky, yet there are few non-blocky grains that record large degrees of internal misorientation (Fig. 6C-D). The CSD profile of upper chromitite crystals is distinct from those of the lower chromitite in that there is no subtle fan-shaped array at larger grain sizes (> 0.2 mm; Fig. 6E). Like lower chromitite CSD profiles, however, there is a slight convex concave pattern at smaller grain sizes (< 0.2 mm), which is consistent with small degrees of Ostwald Ripening (Marsh 1988).

There is negligible inter- and intra-grain chemical variation in upper chromitite crystals. The chromite crystals have 23.4-26.2 mol.% Mg#, 71.8-75.0 mol.% Cr#, and 2.7-3.3 wt.% TiO_2. The single plagioclase-hosted crystal has the lowest Cr# and highest Mg# values measured in this unit. Like the lower chromitite crystals, Mg# values decrease with increasing Cr# values; however, upper chromitite crystals have statistically significantly lower Mg# and higher Cr# concentrations (Fig. 8). Moreover, upper chromitite crystals have higher V, Sn, and Mn concentrations than lower chromitite crystals.

Table 2: Compositions used for Magma Chamber Simulator modelling. Parent melt compositions are from Barnes *et al.* (2010) and footwall compositions are from Maier and Eales (1997).

[1]*Role:*	Replenishing melts		Wall rock cumulates						
Explanation:	average composition	Calculated from averages	Average UA 647.9, 649.4, and 652.9		Average IM 801, 810.1, & 818		Average IN 811.73, LK7 1389.7, EK22 272,25, & H3 1054.1		Impala 788.8
[2]*Name:*	B1	60B1:40B2	lnor	h-lnor	nor	h-nor	mnor_1	h-mnor_1	mnor_2
wt% SiO_2	56.4	54.1	49.2	48.3	50.5	49.6	50.6	49.7	52.3
wt% TiO_2	0.34	0.51	0.06	0.06	0.09	0.08	0.09	0.09	0.17
wt% Al_2O_3	12.0	13.5	28.7	28.1	22.9	22.4	19.2	18.8	12.8
wt% Fe_2O_3	1.36	1.42	0.05	0.05	0.09	0.09	0.18	0.18	0.69
wt% Cr_2O_3	0.14	0.10	0.05	0.05	0.20	0.20	0.21	0.21	0.34
wt% FeO	8.34	8.97	1.94	1.90	3.99	3.92	5.08	4.98	6.91
wt% MnO	0.18	0.19	0.02	0.02	0.02	0.02	0.10	0.10	0.17
wt% MgO	12.0	9.9	3.5	3.5	8.6	8.5	12.9	12.6	17.5
wt% NiO	0.04	0.03	0.01	0.01	0.02	0.02	0.04	0.04	0.05
wt% CaO	6.6	8.2	14.0	13.8	11.6	11.4	9.9	9.7	7.8
wt% Na_2O	1.65	1.76	2.18	2.14	1.79	1.76	1.50	1.47	1.11
wt% K_2O	0.99	0.69	0.18	0.17	0.08	0.08	0.05	0.05	0.04
wt% P_2O_5	0.08	0.11	0.02	0.02	0.01	0.01	0.04	0.04	0.01
wt% H_2O	0.10	0.50	0.08	1.96	0.03	1.91	0.10	1.98	0.20
Initial T °C	1370	1285	1165	975	1195	985	1160	985	1105

[1] Replenishing melt compositions have been equilibrated in alphaMELTS 1.9 at their liquidus and ΔFMQ. Footwall compositions were initially equilibrated at 800°C and ΔFMQ. [2] lnor = leuconorite, nor = norite, mnor = melaonrite, h- = hydrous.

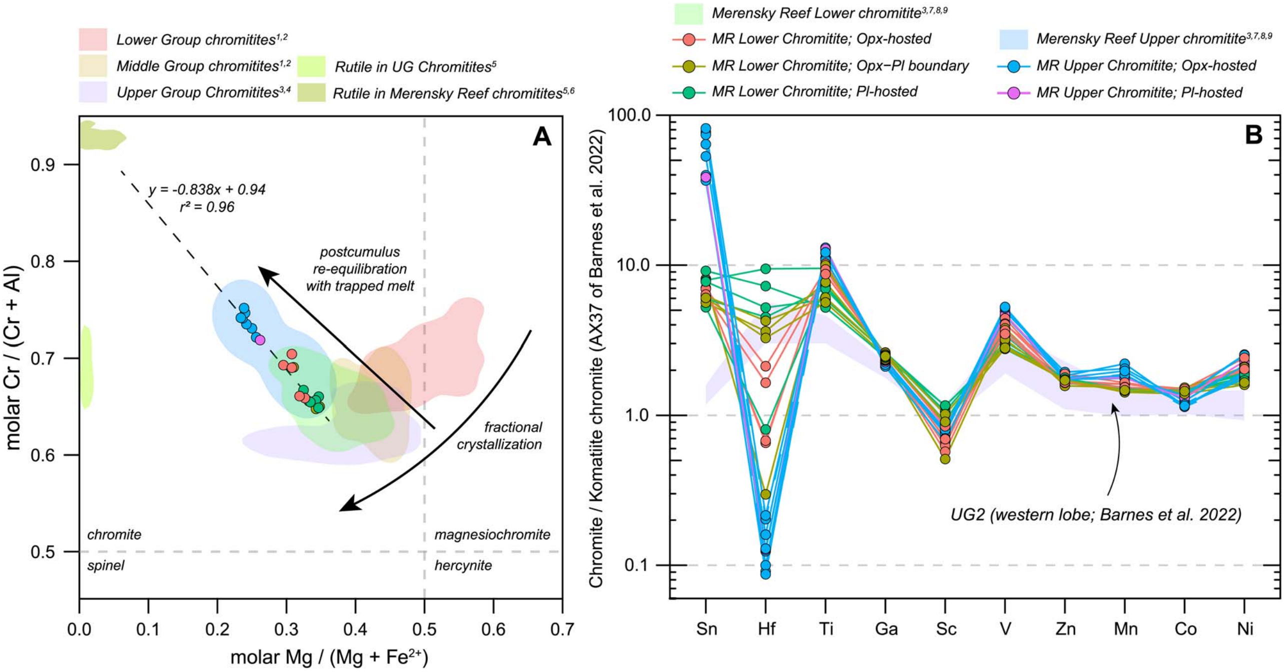

Fig. 8. A. Molar Mg# values *versus* Cr# values for chromite crystals. Upper chromitite crystals have relatively lower Mg# and higher Cr# values compared with lower chromitite crystals. This pattern is consistent with those determined from other studies on the Merensky chromitites and can be explained through postcumulus reaction with residual trapped liquids (Barnes *et al.* 2022). Conversely, massive chromitites in the Critical Zone display trends that are overall more consistent with that expected of fractional crystallization (Yudovskaya and Kinnaird 2010). Rutile compositions from the UG and Merensky chromitites are underlain, where Merensky rutile has relatively high Cr# values. **B.** Chromite trace element concentrations normalized to komatiite chromite AX37 of Barnes *et al.* (2022) underlain by the field of UG2 chromite in the western lobe (Barnes *et al.* 2022). [1] Hatton and von Gruenewaldt (1985), [2] Naldrett *et al.* (2009), [3] Barnes *et al.* (2022), [4] Langa *et al.* (2021), [5] Zaccarini *et al.* (2021), [6] Scoon and Costin (2018), [7] this study, [8] S-J. Barnes unpub, [9] Vukmanovic *et al.* (2013).

The hanging-wall pyroxenite is a medium-grained orthopyroxenite with no obvious compositional or graded layering. It comprises an interconnected network of subhedral cumulus orthopyroxene (~ 65-75%) and intercumulus plagioclase (~ 15-25%) with traces of interstitial clinopyroxene, phlogopite, quartz, and sulfides (ESM 3v). Clinopyroxene sometimes occurs as relatively coarse-grained oikocrysts (up to 1 cm in diameter). As in the central pyroxenite, EPMA analyses of orthopyroxene at the base of the hanging-wall pyroxenite show it to be relatively Mg-rich and Cr-poor where proximal to chromite (Fig. 3A-B). The base of the unit contains very few chromite crystals and a relatively high proportion of sulfides that consist of

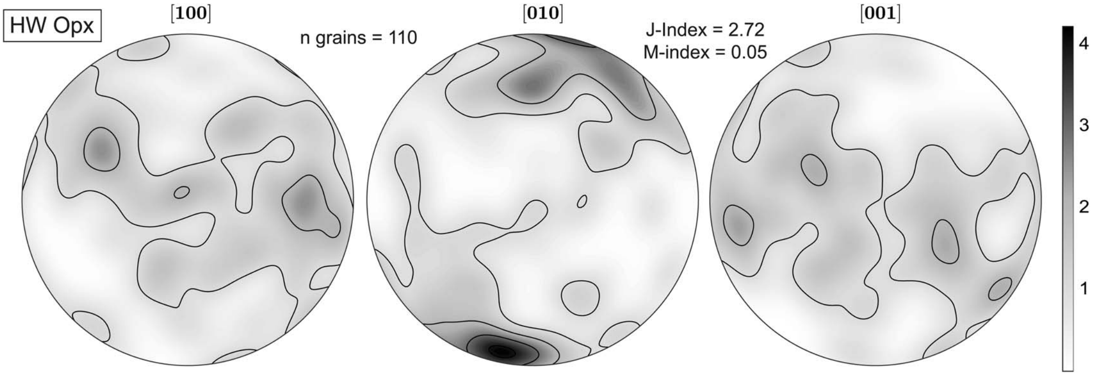

Fig. 9. Lower hemisphere, equal-area pole figures of the [100], [010], and [001] axes of orthopyroxene crystals (one point per crystal) from the lowermost hanging-wall pyroxenite. Note that the hanging-wall cumulates record a weak planar fabric similar to those of the footwall leuconorite.

loop-textured pentlandite encircling pyrrhotite and associated chalcopyrite.

The fabric of cumulus orthopyroxene yields a similar crystallographic preferred orientation (CPO) to that measured in the footwall silicates and conserves a similar orientation for the [010] axes (*J*-index = 2.74; Fig. 9). As in the footwall, internal misorientation is very limited and pristine magmatic textures are preserved. Clinopyroxene and intercumulus plagioclase do not show extensive markers for plastic deformation, with only rare sub-grains and lattice bending being visible at contacts with other phases.

DISCUSSION

Deposition of the footwall leuconorite

The footwall leuconorite is typical of *Upper Critical Zone* norite in that it comprises laminated, subhedral cumulus plagioclase crystals with subhedral orthopyroxene oikocrysts, adjacent to which intercumulus clinopyroxene generally occurs (Fig. 2B; Eales *et al.* 1991; Maier and Eales 1997; Boorman *et al.* 2004). The weak magmatic fabric exhibited by undeformed cumulus plagioclase is evidence for igneous lamination, whereas there is little evidence for lineation (*e.g.*, absence of maxima at the [100] axis; Cheadle and Gee 2017). Similar fabrics have been recorded in cumulus plagioclase-bearing units of the Skaergaard (Holness *et al.* 2017), Rum (Cheadle and Gee 2017), and Stillwater (Jenkins *et al.* 2022) intrusions as well as elsewhere in the Bushveld Complex (Vukmanovic *et al.* 2019; Smith *et al.* 2023). Orthopyroxene oikocrysts define a fabric that is like that of cumulus plagioclase, indicating that both silicates record the same magmatic event. The evidence is consistent with cumulus plagioclase and, by extension, orthopyroxene having accumulated through gravitational settling in a stagnant or weakly-flowing melt (Henry *et al.* 2021), followed by postcumulus overgrowth of orthopyroxene (Barnes *et al.* 2016). Evidence for minor plastic deformation occurred later as a result of crystal loading and compaction of the cumulates (Henry *et al.* 2021).

Cumulus plagioclase crystals show no systematic compositional zoning or change in composition with proximity to the anorthosite (Fig. 10A). However, their compositional zoning patterns diversify at the leuconorite-anorthosite contact (Fig. 4B). This occurs in conjunction with orthopyroxene oikocrysts with relatively lower Mg$\#_{opx}$ values (Fig. 3A) as well as a relative increase in the modal abundance of clinopyroxene and accessory phases (Fig. 11A). This pattern in Mg$\#_{opx}$ has been reported in the footwall units at the Union, Impala Platinum, and Rustenburg Mines (Naldrett *et al.* 1986; Schurmann 1993; Cawthorn 1996). Wilson *et al.* (1999) did not identify this trend in a sequence without the footwall anorthosite at the Rustenburg Platinum Mine but did highlight that Mg$\#_{opx}$ decreases as whole-rock Zr contents increase. This trend was initially ascribed to differentiation (Naldrett *et al.* 1986; Schurmann 1993; Maier and Eales 1997), yet as An content remains constant, it was later proposed to be a result of re-equilibration with variable portions of trapped liquid (Cawthorn 1996; Wilson *et al.* 1999).

Zoning of Mg^{2+} and Fe^{2+} is not often preserved in ferromagnesian cumulates of layered intrusions due to the rapid diffusion rates of these divalent elements (Barnes *et al.* 2016). In contrast, Cr^{3+} and Ti^{4+} diffuse relatively slowly, such that any zoning of these elements could be preserved. For this reason, Barnes (1986b) argued that orthopyroxene-rich cumulates with variable Cr contents for a narrow Mg# range are probably the result of differentiation, whereas orthopyroxene-rich cumulates with narrow Cr contents for a variable Mg# range are probably the result of variable degrees of trapped liquid shift. The effect of trapped liquid shift between 60:40 mixtures of measured plagioclase (An_{80}) orthopyroxene (Mg_{81}) and variable proportions of evolved B1 melt (ECBV105 of Barnes *et al.* 2010) was tested by modelling batch crystallization of spinel-free hypothetical cumulates close to their solidus at 2 kbar and ΔFMQ using alphaMELTS 1.9 (Ghiorso and Sack 1995; Jenkins and Mungall 2018). The final vector is drawn by connecting the original and final 're-equilibrated' orthopyroxene compositions (see supplementary materials). Log $D_{Cr}^{opx/liq}$ was parametrized as -4.59 + 8100 / Temperature (K) and $D_{Cr}^{cpx/liq}$ was taken as 1.7 × $D_{Cr}^{opx/liq}$ (following Barnes 1986a, 1986b).

Results of the modelling show that Mg$\#_{opx}$ can be lowered 1.0, 3.6, and 7.1 mol.% in the presence of 5%, 10%, and 20% trapped liquid, respectively, and Cr contents slightly decrease (Fig. 12), consistent with the results of Barnes (1986b). Orthopyroxene crystals from the leuconorite have variable Cr contents for narrow Mg$\#_{opx}$ values, consistent with the effects of differentiation and subsequent Mg^{2+}-Fe^{2+} diffusion (Barnes 1986b). The relatively lower Mg$\#_{opx}$ values for orthopyroxene crystals at the leuconorite-anorthosite contact can, therefore, be ascribed to orthopyroxene re-equilibrating with up to 10% trapped liquid. These results are consistent with the observed increase in the modal abundance of intercumulus pyroxene and accessory minerals at this transition as well as modal trapped liquid estimates for the Upper Critical Zone norite (1-10%; Cawthorn and Walsh 1988; Cawthorn 1996; Wilson *et al.* 1999; Yao *et al.* 2021). Moreover, as disseminated sulfides subtly concentrate directly above the leuconorite, the composition of orthopyroxene may have been further influenced

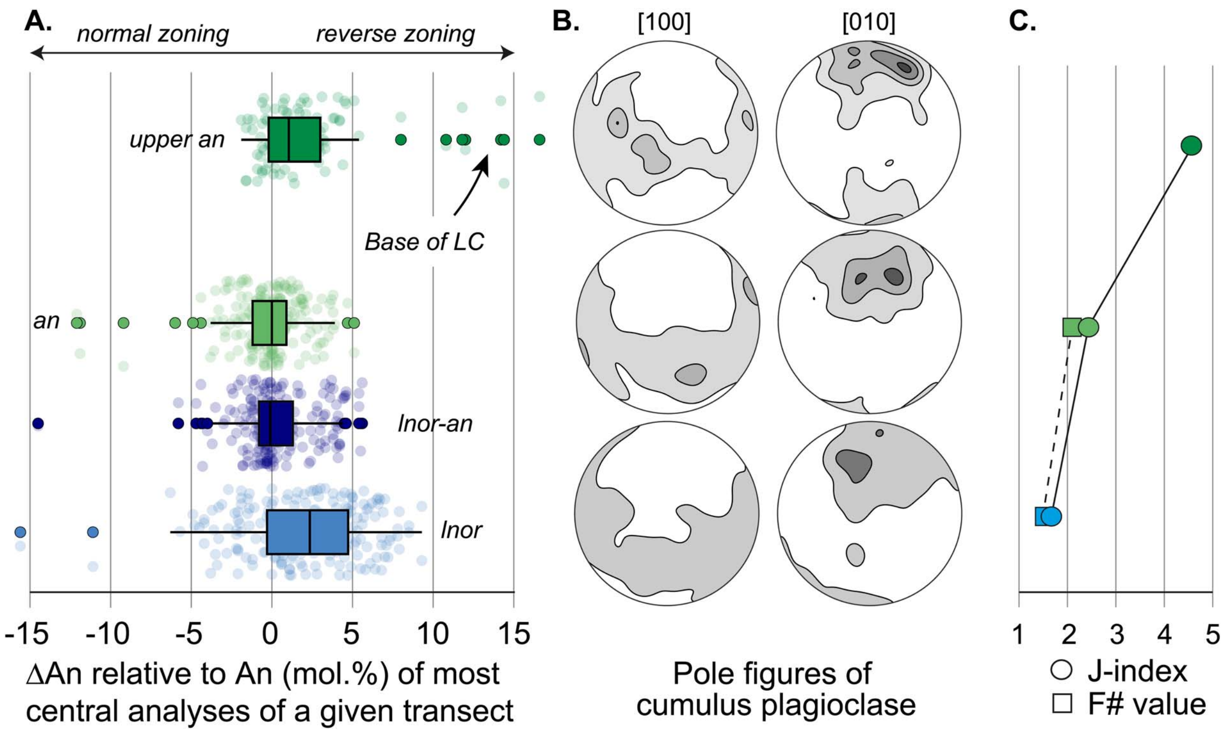

Fig. 10. Plagioclase compositions and microtextures in the Merensky Reef footwall. **A.** Box-and-whisker diagrams of ΔAn content relative to the An content of the most central analytical point of a given transect. Note the anomalous reverse zoning of plagioclase in the upper anorthosite (*i.e.,* directly beneath the lower chromitite). **B.** [100] and [010] pole figures of cumulus plagioclase. **C.** *J*-index and F# values of cumulus plagioclase throughout the footwall. Note that the strength of the CPO increases with proximity to the reef.

by Fe-Ni exchange with sulfide melt, though we presently do not have the data to confirm this.

Formation of the footwall anorthosite

In many parts of the western lobe of the Bushveld Complex, the Merensky Reef is underlain by an anorthosite of variable thickness (Eales *et al.* 1988; Viring and Cowell 1999). In the Critical Zone, anorthosite typically occurs at the top of interlayered packages of pyroxenite, norite, and anorthosite (Kruger and Marsh 1985; Eales *et al.* 1986; Maier and Eales 1997; Cawthorn 2002; Seabrook *et al.* 2005; Veksler *et al.* 2015; Hunt *et al.* 2018). As a result, anorthosite layers are often overlain by PGE-rich chromitite seams that tend to occur at the base of these units (Eales *et al.* 1990; Scoon and Teigler 1995; Van der Merwe and Cawthorn 2005; Maier and Barnes 2024). This spatial association between anorthosite and chromitite is recognized in other layered intrusions, such as Rum (Scotland; O'Driscoll *et al.* 2009), Stillwater (USA; Marsh *et al.* 2021), and Penikat (Finland; Maier *et al.* 2018). The origin of the Critical Zone cycles has been ascribed to magma replenishment, during which the replenishing melt(s) may have thermally, mechanically, and (or) chemically interacted with resident cumulates (Eales *et al.* 1986, 1988; Maier and Eales 1997; Viljoen 1999; Roberts *et al.* 2007; Scoon and Costin 2018; Mitchell *et al.* 2019; Kruger and Latypov 2021; Latypov *et al.* 2022).

In this study, the anorthosite is relatively thin compared to footwall anorthosite elsewhere at the Rustenburg Platinum Mines (Viljoen and Hieber 1986; Eales *et al.* 1988). Cumulus plagioclase at the base of the anorthosite displays normal, reverse, and oscillatory zoning, whereas plagioclase crystals directly beneath the lower chromitite are often reversely zoned (Figs. 3D and 4B). Reversely zoned plagioclase are commonplace in the Upper Critical Zone (Maier 1992; Maier and Eales 1997; Robb and Mungall 2020, Maier *et al.* 2021a), and it appears to become most pronounced in 'pure' anorthosite rind that occurs directly beneath the lower chromite (Smith *et al.* 2021; Latypov *et al.* 2023); a feature also described encircling boulders of the Boulder Bed (Smith *et al.* 2023) and in the Medium-Grained Anorthosite member of the Stillwater Complex (Baker and Boudreau 2019). This diversity of plagioclase zoning provides evidence of a complex and changing melt composition in this layer compared to the underlying leuconorite, which has relatively limited zoning of cumulus plagioclase. In the leuconorite, the weakly laminated and largely undeformed plagioclase crystals, with no discernible lineation, are consistent with crystal settling in a quiescent melt column (Cheadle and Gee 2017). However, the strength of the plagioclase lamination increases upwards through the footwall anorthosite (*i.e.,* towards the lower chromitite; Fig. 10B-C) and this requires further explanation.

Sinuous networks of sulfides and intercumulus pyroxenes traverse the anorthosite and blanket the leuconorite (Fig. 11A; Cawthorn 1999; Barnes and Maier 2002; Godel *et al.* 2006; Naldrett *et al.* 2009; Smith *et al.* 2021). This is compelling evidence that the anorthosite was relatively permeable at the time of sulfide melt percolation, while the underlying leuconorite was virtually solidified (Smith *et al.* 2021). Intercumulus pyroxenes, quartz, and phlogopite are relatively abundant in the uppermost centimeter of the leuconorite and remain abundant throughout the sinuous networks (Fig. 11A). Very fine-grained chromite occurs at the margins of orthopyroxene crystals throughout the upper leuconorite and, though less frequent, persist in the sinuous networks (Fig. 11). These crystals may form during the dissolution of Cr-bearing orthopyroxene (Marsh *et al.* 2021) and may then themselves dissolve as the reaction with replenishing melt progresses – their persistence in the sinuous networks is

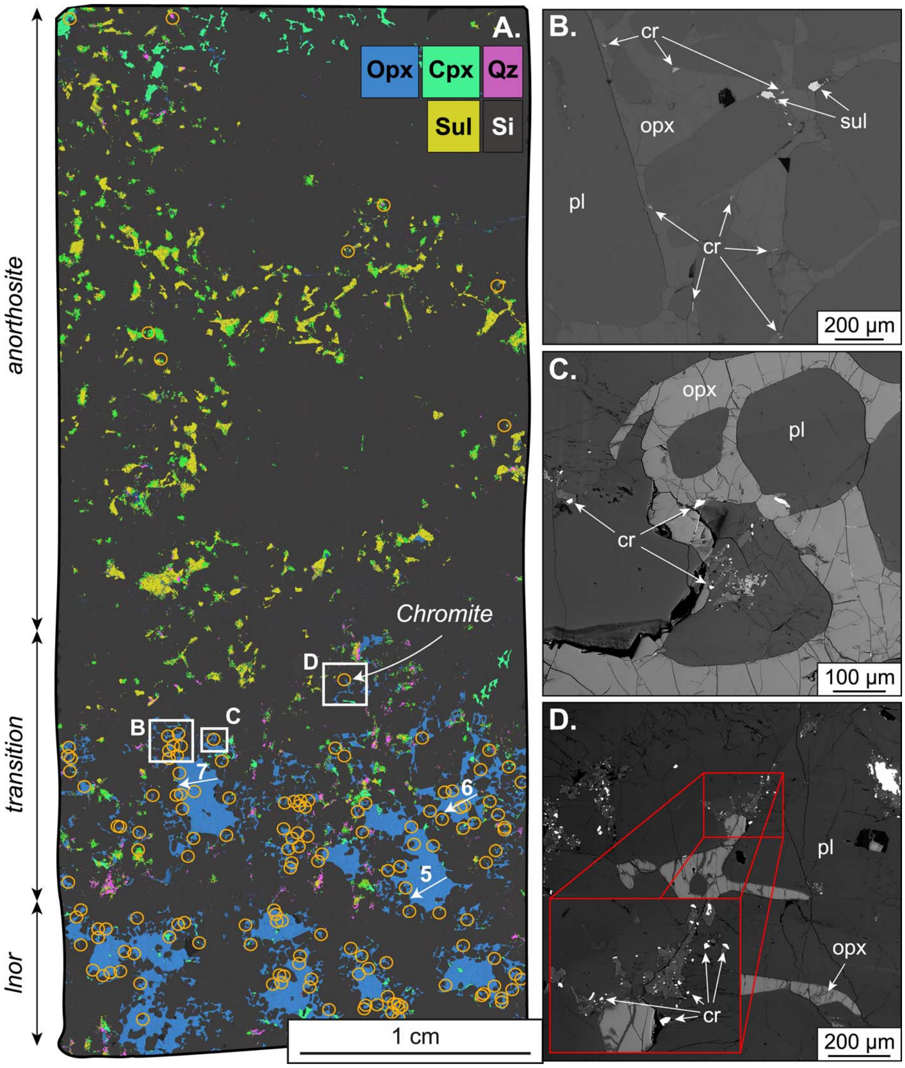

Fig. 11. Nature of chromite (cr) crystals in the Merensky footwall. **A.** Si-Mg-Ca-S element map of section C1, which intersects the leuconorite-anorthosite transition. Note the more poikilitic nature of orthopyroxene, relative increase in intercumulus clinopyroxene, quartz (qz), and sulfide (sul) at the transition, as well as the distribution of very fine-grained chromite (circled by orange rings). Arrows correspond to EPMA transects. **B-D.** Backscattered electron images of very fine-grained chromite at the margins of orthopyroxene (opx) oikocrysts in the transition zone.

evidence that Cr is mobile. The footwall anorthosite has ~ 1% sulfide, and so the downward percolation of sulfide melt cannot alone account for the upward migration of relatively larger proportions of trapped silicate melt. As such, we hypothesize that relatively buoyant Cr-bearing silicate melt generated during this reaction migrated upwards, aided by the downward percolation of relatively dense sulfide melt. Several studies of the Merensky Reef have shown that incompatible trace element concentrations peak stratigraphically above peaks in chalcophile element concentrations (Lee 1983; Cawthorn 1996; Wilson *et al.* 1999; Barnes and Maier 2002), which has also been ascribed to the upward displacement of evolved silicate melt aided by downgoing sulfide melt (Cawthorn and Boerst 2006).

Our observations indicate that the anorthosite seemingly cannot be explained by gravitational processes alone. Instead, the data are more consistent with a model whereby the anorthosite formed as a restite of partial melting during chamber replenishment (Eales *et al.* 1988; Roberts *et al.* 2007; Mungall *et al.* 2016). This process could generate enhanced porosity allowing for the migration of sulfide and silicate melts. One-dimensional heat flow models (Ehlers 2005) indicate that a stagnant melt at 1300°C is not able to raise the temperature of floor rocks above 1200°C unless the floor rocks are already hot (> 1000°C) and (or) the melt column is excessively hot (> 1500°C) or thick (> 1 km). Thus, for melting to proceed, the heat of the overlying melt must be sufficiently sustained for prolonged periods of time via continuous replenishment. It should be noted that alternative models have been proposed for the anorthosite underlying the Merensky Reef, including reactive porous flow (Nicholson and Mathez 1991; Mathez 1995; Marsh *et al.* 2021; Maier *et al.* 2021b).

To provide additional constraints on the viability of footwall melting by replenishing melt, a series of assimilation-fractional crystallization thermodynamic models at 2 kbar pressure were performed using Magma Chamber Simulator (Bohrson *et al.* 2014, 2020). The replenishing melt was modelled as B1 or 60:40 B1:B2 (Table 2; Barnes and Maier 2002; Barnes *et al.* 2010), which were both equilibrated at ΔFMQ. The footwall compositions were taken from data of Maier and Eales (1997) who studied the UG2-Merensky Reef interval along strike in the western lobe. These included: (i) leuconorite (lnor) with ~ 3.5 wt.% MgO (average of Union 647.9, 649.4, and 652.9); (ii) norite (nor) with ~ 8.6 wt.% MgO (average of IN 811.73, LK7 1389.7, EK 22 272.25, and H3 1054.1);

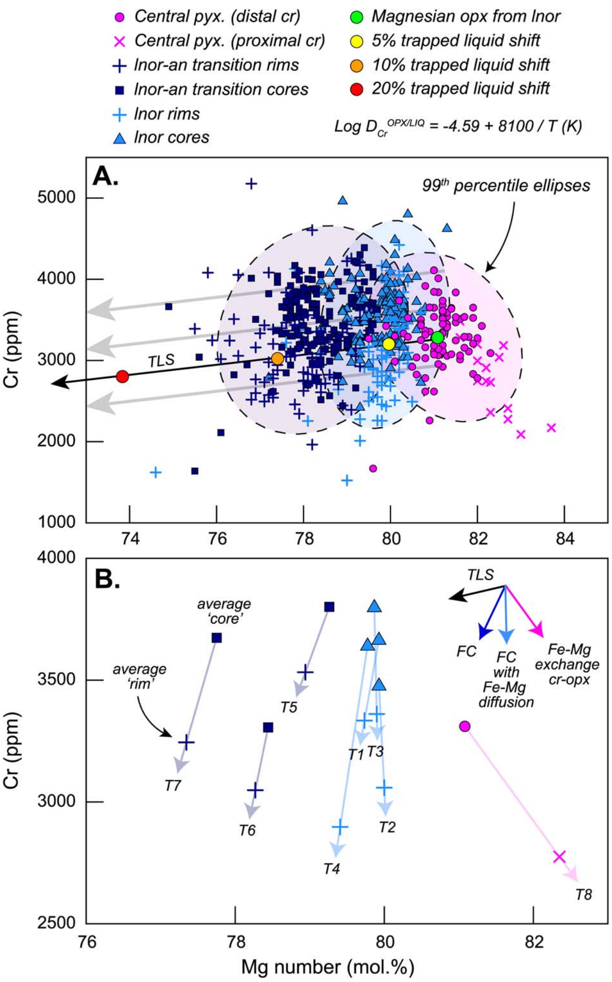

Fig. 12. Composition of orthopyroxene and nature of the leuconorite-anorthosite (lnor-an) transition. **A.** Orthopyroxene core and rim compositions from the footwall and central pyroxenite (pyx) underlain by 99th percentile ellipses. The colored circles and arrows highlight the compositional effect of trapped liquid shift (TLS), whereby the Mg# values of poikilitic orthopyroxene at the leuconorite-anorthosite transition may have been lowered during interaction with up to 10% trapped interstitial liquid. **B.** Average core and rim compositions for individual orthopyroxene crystals analyzed in the footwall lithologies and central pyroxenite. Rim compositions were averaged from the outermost 20% analytical points. The compositions of orthopyroxene crystals in the footwall are consistent with variable degrees of fractional crystallization (FC), Fe-Mg diffusion, and TLS, whereas orthopyroxene in the central pyroxenite has undergone chemical exchange with chromite.

(iii) melanorite (mnor) with 11.6 wt.% MgO (mnor; average IM 801, 810.1, and 818); (iv) highly melanocratic (mnor2) norite with 17.6 wt.% MgO (IM788.8 at Impala IM). Prior to modelling, FeO/Fe_2O_3 was calculated for each footwall composition at 800°C and ΔFMQ, and hydrous equivalents (denoted as *h*-) with ~ 2 wt.% H_2O were also produced (Table 2). At the beginning of the simulations, each floor rock was set slightly above solidus temperature so that 8-10 wt.% of interstitial melt was present – 10 wt.% of interstitial melt was set as a percolation threshold for the floor rock melt to exit the residue.

Since in Magma Chamber Simulator all heat is distributed evenly in an input mass of wall rock (here floor rock), we varied its initial mass between 10-50 units (relative to initial melt mass of 100 units, *i.e.*, melt:footwall ratios of 10-2). This can be considered to simulate gradational changes in footwall composition due to uneven heat distribution. In nature, the thickness of the affected zone is governed by kinetic processes (such as conduction) that are not considered by thermodynamics modeling. Simulations with low floor rock mass correspond to situations of inefficient heat conduction and melting processes taking place in the close vicinity of the replenishment magma. Each simulation was conducted using 2-5°C temperature decrements for the replenishment magma. The models with 2 °C decrements were preferred because they provided a better resolution to study the melting reactions in the footwall. Larger decrements were used for simulations with higher floor rock mass, where such resolution was not crucial. The results are summarized in Table 3 and complete model output files are provided in the online supplementary repository.

Leuconorite and norite floor rocks may react with replenishing melts to form an anorthositic restite, particularly when the system is water-poor, when there is a relatively small volume of reactive floor rock, or when the replenishing melt is relatively primitive (B1; Fig. 13A-D). The resulting restite comprises 84.6-99.7% plagioclase ($\text{An}_{80\text{-}90}$) with accessory olivine ($\text{Fo}_{88\text{-}94}$) and Cr-spinel (Table 3). The relative proportions of olivine and Cr-spinel increase in water-rich scenarios and when the replenishing melt is relatively primitive. Olivine progressively replaces orthopyroxene in the residue and will later itself become consumed as the reaction progresses. In each scenario, the replenishing melt first becomes saturated in orthopyroxene ($\text{Mg}_{85\text{-}88}$) and then Cr-spinel. The initial floor rock melts that form contain ~ 0.84 and 6.0 wt.% H_2O for water-poor and water-rich scenarios, respectively. Such water combined with any halogens liberated from accessory phases (*e.g.,* apatite, mica, amphibole), although not considered in the simulations, may constitute a burst of volatiles at the level of the nascent Merensky Reef (Boudreau *et al.* 1986). The absence of olivine at the study location suggests that the system was relatively dry and (or) that the olivine was consumed by some reaction. The latter is feasible considering the inferred heightened proportion of trapped melt (Fig. 12) as well as the presence of quartz, clinopyroxene, and spinel – products in reactions between plagioclase and ferromagnesian minerals.

It is emphasized that although the used modeling scenario was assimilation-fractional crystallization, we did not aim to model the assimilation process itself, nor its consequences to the replenishment melt. The focus was on how the heat (both sensible and latent) released by the crystallizing replenishing melt could modify the resident cumulates. Possible blanketing of the resident cumulates by crystallization does not significantly hinder this process because the reaction zone appears to be quite thin (cm-scale), whereas the replenishing melt is presumed to be at least 20 m thick (see *Section* 5.4). It is argued that the sinuous channels record intercumulus melt exchange between the melt column and underlying porous cumulates and, as such, some crystals had likely formed at the cumulate-melt interface as this reaction progressed. This is further supported by evidence for trapped liquid shift in the reef stratigraphy as discussed in *Section* 5.5.

In summary, resident leuconoritic cumulates can readily react with replenishing melt to become anorthosite restite. This is regardless of the water concentration of the system, the volume of reactive cumulates, or the nature of the replenishing melt. Anorthosite restites may also derive from more noritic cumulates, yet the higher degrees of consumption required may only be attained when there are small volumes of floor rocks that react (< 20 g of cumulate to 100 g of replenishing melt) or when the temperature of the overlying melt is sustained for extended periods, perhaps by way of progressive replenishment.

Table 3: Summary of selected Magma Chamber Simulator outputs showing the formation of different rock types by reconstitution of noritic floor rocks. All model outputs are available in the online supplementary repository.

Initial floor rock [1]	Replenishing melt (Mg#)	Initial mass of floor rock (mu)	Final floor rock temp (°C)	Relative mass of floor rock assimilated (%)	Residual floor rock	Residual floor rock assemblage (%)				Final Mg#[2] of Rpl melt	Replenishing melt cumulate assemblage (mu)	
							ol (Fo)	opx (Mg#)	pl (An)	Cr-spn	opx (final Mg#)	Cr-spn
lnor	60B1:40B2 (65)	10	1263	33.4	anorthosite			99.7 (82)	0.3	63.9	2.2 (85)	
lnor	60B1:40B2 (65)	20	1256	27.3	anorthosite	0.4 (90)		99.0 (81)	0.6	63.2	3.7 (85)	
lnor	60B1:40B2 (65)	30	1248	23.0	anorthosite	3.0 (89)		96.7 (81)	0.3	62.6	4.7 (84)	0.01
lnor	60B1:40B2 (65)	40	1245	21.5	anorthosite	3.4 (89)		96.3 (80)	0.3	62.1	5.8 (84)	0.03
lnor	60B1:40B2 (65)	50	1241	20.1	anorthosite	3.7 (88)		96.0 (80)	0.3	61.5	6.8 (84)	0.05
h-lnor	60B1:40B2 (65)	10	1248	42.9	anorthosite			96.4 (90)	3.6	63.4	3.2 (85)	
h-lnor	60B1:40B2 (65)	20	1213	39.6	anorthosite	0.5 (90)		95.8 (89)	3.7	62.3	5.3 (84)	0.03
h-lnor	60B1:40B2 (65)	30	1203	38.0	anorthosite	1.2 (90)		95.3 (89)	3.5	61.3	7.4 (83)	0.07
h-lnor	60B1:40B2 (65)	40	1187	36.1	anorthosite	1.9 (89)		94.8 (89)	3.3	60.3	9.1 (83)	0.10
h-lnor	60B1:40B2 (65)	50	1157	34.1	anorthosite	2.7 (88)		94.2 (88)	3.0	59.5	10.5 (82)	0.13
nor	60B1:40B2 (65)	10	1264	72.2	troctolite	11.1 (93)		84.2 (85)	4.7	63.9	3.0 (85)	
nor	60B1:40B2 (65)	20	1257	52.3	olivine norite	3.9 (91)	17.7 (90)	76.1 (83)	2.3	63.2	4.5 (85)	<0.01
nor	60B1:40B2 (65)	30	1251	38.1	norite	1.7 (88)	23.3 (89)	73.4 (81)	1.5	62.6	5.2 (84)	0.02
nor	60B1:40B2 (65)	40	1247	30.3	norite	1.1 (87)	25.2 (87)	72.4 (80)	1.2	62.0	5.9 (84)	0.03
nor	60B1:40B2 (65)	50	1244	26.5	norite	1.0 (86)	25.9 (87)	72.0 (80)	1.1	61.6	6.6 (84)	0.04
nor	B1 (70)	10	1296	82.0	anorthosite			85.2 (90)	14.8	68.7	5.5 (87)	
nor	B1 (70)	20	1279	76.2	anorthosite	4.6 (94)		84.6 (88)	10.8	67.1	9.8 (87)	
nor	B1 (70)	30	1275	69.1	troctolite	9.8 (93)		83.4 (87)	6.9	65.6	13.4 (85)	
nor	B1 (70)	40	1259	54.3	troctolite	12.8 (91)	3.4 (90)	80.7 (85)	3.0	63.9	15.6 (85)	
nor	B1 (70)	50	1245	39.9	olivine norite	8.8 (88)	12.6 (88)	76.6 (84)	2.0	62.6	16.6 (84)	
h-nor	60B1:40B2 (65)	10	1250	53.0	troctolite	20.7 (88)		74.9 (88)	4.4	63.2	3.4 (85)	
h-nor	60B1:40B2 (65)	20	1228	44.7	troctolite	22.1 (86)		75.0 (87)	2.9	62.0	5.7 (84)	0.03
h-nor	60B1:40B2 (65)	30	1197	40.0	troctolite	22.9 (85)		74.9 (87)	2.2	61.1	7.5 (83)	0.07
h-nor	60B1:40B2 (65)	40	1190	39.0	troctolite	23.0 (85)		74.9 (87)	2.1	60.1	9.4 (83)	0.11
h-nor	60B1:40B2 (65)	50	1160	36.2	troctolite	22.6 (84)	1.0 (85)	74.5 (86)	1.8	59.5	10.5 (82)	0.14
mnor	60B1:40B2 (65)	10	1261	76.9	olivine norite	36.9 (91)	20.9 (91)	36.1 (86)	6.2	63.8	3.4 (85)	
mnor	60B1:40B2 (65)	20	1254	49.6	olivine norite	12.8 (88)	34.8 (89)	50.2 (83)	2.2	62.9	4.8 (84)	0.01
mnor	60B1:40B2 (65)	30	1247	36.5	olivine norite	9.2 (87)	36.5 (88)	52.8 (82)	1.6	62.2	5.8 (84)	0.03
mnor	60B1:40B2 (65)	40	1240	28.1	olivine norite	7.8 (86)	37.0 (87)	53.9 (81)	1.3	61.7	6.5 (84)	0.04
mnor	60B1:40B2 (65)	50	1238	25.3	olivine norite	7.4 (85)	37.2 (86)	54.2 (80)	1.2	61.2	7.5 (83)	0.06
h-mnor	60B1:40B2 (65)	10	1245	57.0	troctolite	44.4 (87)		51.4 (88)	4.1	63.3	3.4 (85)	
h-mnor	60B1:40B2 (65)	20	1226	47.8	olivine norite	37.5 (86)	6.0 (87)	53.7 (88)	2.9	62.2	5.7 (84)	0.03
h-mnor	60B1:40B2 (65)	30	1209	43.1	olivine norite	34.1 (85)	9.3 (86)	54.1 (88)	2.5	61.2	7.7 (83)	0.07
h-mnor	60B1:40B2 (65)	40	1190	40.0	olivine norite	32.2 (85)	11.1 (86)	54.4 (88)	2.3	60.5	9.2 (83)	0.10
h-mnor	60B1:40B2 (65)	50	1159	37.1	olivine norite	30.8 (84)	12.4 (85)	54.7 (88)	2.1	59.8	10.6 (82)	0.14
h-mnor	B1 (70)	10	1265	78.7	troctolite	58.7 (90)		26.5 (90)	14.8	67.2	5.0 (87)	
h-mnor	B1 (70)	20	1271	75.4	troctolite	54.2 (90)		33.7 (90)	12.1	65.8	8.8 (86)	0.03
h-mnor	B1 (70)	30	1255	60.1	troctolite	45.3 (88)		49.7 (89)	5.0	64.8	10.6 (86)	0.06
h-mnor	B1 (70)	40	1228	49.4	troctolite	39.0 (86)	4.5 (87)	53.5 (88)	3.0	63.8	12.2 (85)	0.09
h-mnor	B1 (70)	50	1215	45.2	olivine norite	35.7 (86)	7.7 (86)	54.0 (88)	2.7	63.0	14.0 (84)	0.13
mnor2	60B1:40B2 (65)	10	1254	58.3	orthopyroxenite	0.4 (88)	95.4 (88)		4.2	64.9	3.4 (86)	<0.01
mnor2	60B1:40B2 (65)	20	1256	58.2	orthopyroxenite	0.1 (88)	95.6 (88)		4.3	63.6	6.4 (85)	0.05
mnor2	60B1:40B2 (65)	30	1250	50.6	orthopyroxenite		87.4 (87)	9.2 (86)	3.3	62.5	8.5 (84)	0.08
mnor2	60B1:40B2 (65)	40	1239	36.6	norite		77.3 (86)	20.4 (83)	2.2	61.7	9.4 (84)	0.10
mnor2	60B1:40B2 (65)	50	1233	31.7	norite	0.1 (86)	74.7 (86)	23.2 (82)	2.0	61.0	10.7 (84)	0.12
mnor2	B1 (70)	10	1297	61.1	orthopyroxenite	3.4 (89)	93.2 (88)		3.4	68.8	4.1 (87)	
mnor2	B1 (70)	20	1300	60.7	orthopyroxenite	3.0 (89)	93.5 (88)		3.5	67.3	7.5 (87)	
mnor2	B1 (70)	30	1300	60.6	orthopyroxenite	2.9 (89)	93.6 (88)		3.5	65.9	10.7 (86)	
mnor2	B1 (70)	40	1281	59.6	orthopyroxenite	1.8 (89)	94.4 (88)		3.8	64.7	13.3 (85)	
mnor2	B1 (70)	50	1256	58.2	orthopyroxenite		95.7 (88)		4.3	63.8	15.5 (85)	

[1] lnor = leuconorite, nor = norite, mnor = melanorite, h- = hydrous

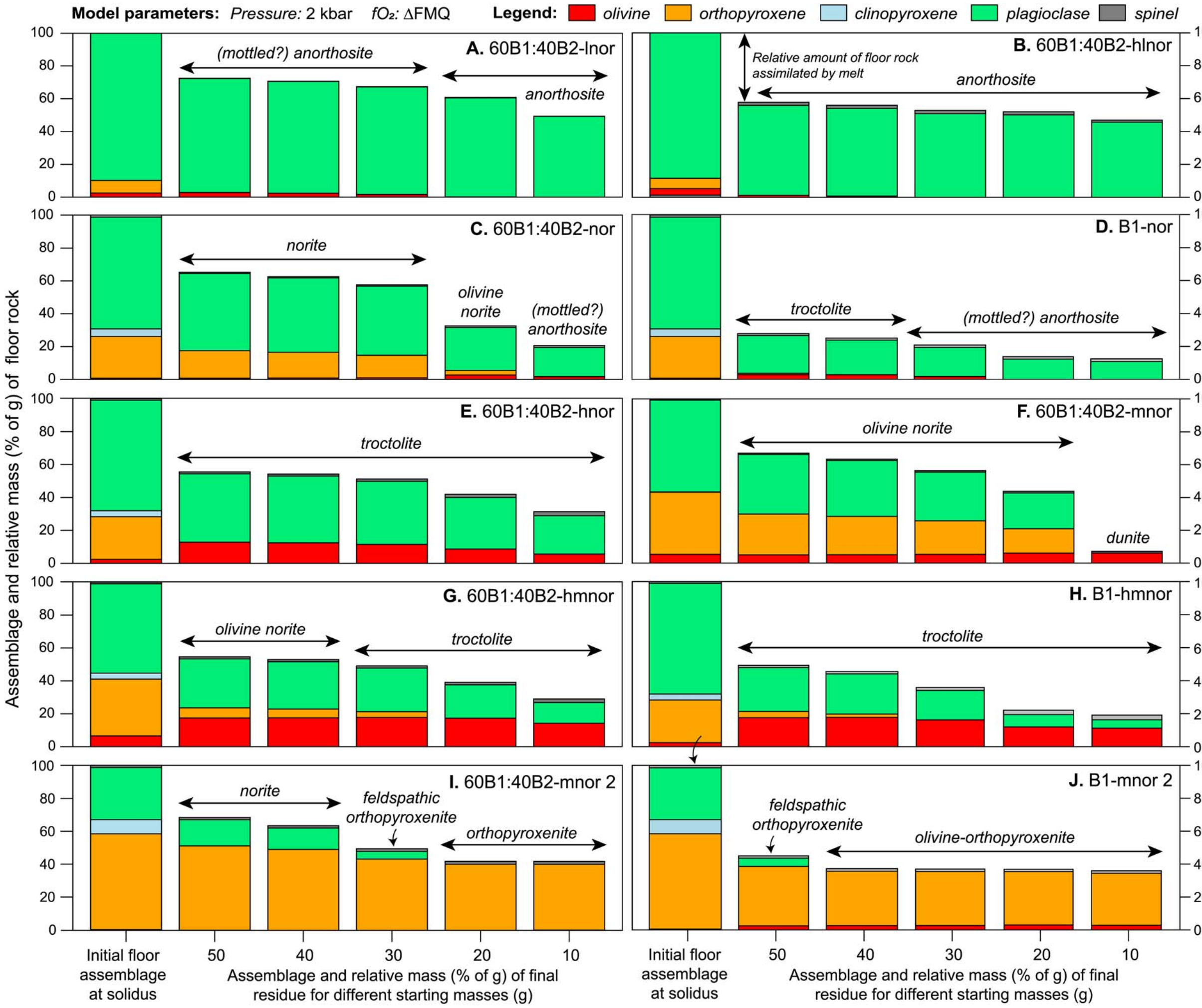

Fig. 13. Results from Magma Chamber Simulator models (also summarized in Table 3). The diagrams show the final mass (relative to the initial starting mass that has been normalized to 100) and assemblage of the floor rocks following the interaction with replenishing 60B1:40B2 or B1 melt. The illustrated floor rocks include leuconorite (A-B), norite (C-E), melanorite (F-H), and high-Mg melanorite (I-J). Note that this interaction is capable of reconstituting resident noritic cumulates to a restite of anorthosite, norite, troctolite, olivine norite, or orthopyroxenite under different initial conditions. All models are available at doi.org/10.25919/rgb7-ch54.

Formation of alternative lithologies underlying the Merensky reef

Anorthosite is not the only lithology that underlies the Merensky Reef. In the NW and SE of the western lobe of the Bushveld Complex, the Merensky Reef is underlain by troctolite and olivine norite (Viring and Cowell 1999; Roberts *et al.* 2007). At Northam, Roberts *et al.* (2007) ascribed the formation of olivine-bearing footwall lithologies to the reconstitution of norite floor rocks by relatively primitive downward-percolating melt, in a process they termed *troctolitization*. During troctolitization, Cr- and S-saturated B1 melt percolates downward into footwall leuconorite, where it consumes orthopyroxene and precipitates olivine that will later become encased in peritectic orthopyroxene (Roberts *et al.* 2007). Regardless of the true mechanism, reconstitution of noritic-gabbroic cumulates to troctolite may operate in layered intrusions. Examples include: (1) the selvage of troctolite around norite-hosted iron-rich ultramafic pegmatites (Bushveld; Reid and Basson 2002); (2) troctolites in Olivine-bearing Zone I of the Stillwater Complex may have formed by fluid-induced incongruent melting of gabbronorite (Boudreau 1999) or as fractionated cumulates of hybridised melt generated as replenishing melt assimilated partial melts of resident gabbronorite (Jenkins *et al.* 2021); (3) troctolite at the Wavy Horizon of the Rum intrusion may have formed by dissolution of clinopyroxene by infiltrating melt (Holness *et al.* 2007). Moreover, in parts of the eastern lobe, the Merensky Reef is underlain by variably feldspathic orthopyroxenite (Mathez *et al.* 1997; Mitchell *et al.* 2019). Below we discuss the conditions under which olivine norite, troctolite, and orthopyroxenite restites may be produced during chamber replenishment (Table 3).

Norite residues can remain in water-poor scenarios, where noritic or melanoritic floor rocks react with relatively evolved replenishing melt (60:40 B1:B2) and all clinopyroxene is consumed (Fig. 13C, I). In water-rich scenarios and (or) scenarios considering B1 replenishing melt, olivine norite restites are produced as noritic or melanoritic floor rocks are consumed (Fig. 13B, E, F, H). These residues contain variable proportions of olivine (Fo$_{84-91}$), orthopyroxene (Mg#$_{85-91}$), and plagioclase (An$_{80-86}$), with accessory Cr-spinel. Troctolite residues are produced when all orthopyroxene has been replaced by olivine. This occurs in scenarios where noritic or melanoritic floor rocks react with replenishing melt, particularly when the system is water-rich and when the replenishing melt is relatively primitive (Fig. 13D, E, G, H). The troctolite restite contains variable proportions of olivine (Fo$_{84-93}$)

and plagioclase (An_{85-90}) with accessory Cr-spinel and in some cases orthopyroxene (Mg$\#_{85-90}$) where not fully replaced by olivine. These results support the interpretations of Roberts *et al.* (2007) and further demonstrate that olivine-bearing floor rocks can be generated without the need for downward melt percolation. It remains possible that reconstituted troctolitic cumulates can be subjected to a second phase of replenishment-driven reconstitution to produce anorthositic cumulates, like that proposed for the JM Reef of the Stillwater Complex (Jenkins *et al.* 2021).

Orthopyroxenite and feldspathic orthopyroxenite restites may be produced when replenishing melts react with melanorite floor rocks that have orthopyroxene:plagioclase ratios above 1 (Fig. 13I, J). To make orthopyroxenite, the system must be relatively water-poor to avoid the precipitation of significant proportions of olivine, which would instead lead to the formation of olivine-orthopyroxenite or harzburgite. Residual orthopyroxenite contains 87-96% orthopyroxene (Mg$\#_{87-88}$), with accessory Cr-spinel (< 5%), olivine (Fo_{86-89}), and plagioclase (An_{86}). The rarity of orthopyroxenite directly beneath the Merensky Reef perhaps reflects the rarity of *Upper Critical Zone* norites with orthopyroxene:plagioclase ratios above 1.

Implications for the formation of the lower chromitite and its bimodal chromite population

The origin of chromitites in layered intrusions remains intensely debated (Barnes *et al.* 2022; Latypov *et al.* 2024). It is likely that thin chromitite seams, such as the Merensky chromitites, form in a different manner from that of massive chromitites (Scoon and Costin 2018; Barnes *et al.* 2022). Some thin chromitites likely form when replenishing silicate melts (or upwelling volatiles) interact with resident cumulates, liberating auxiliary Al^{3+} and Cr^{3+} from the cumulates to instigate chromite supersaturation (Boudreau *et al.* 1986; Nicholson and Mathez 1991; O'Driscoll *et al.* 2009; Scoon and Costin 2018; Marsh *et al.* 2021). Such a model could explain the abundant very fine-grained chromite crystals in the footwall leuconorite that abruptly vanish at the contact with footwall anorthosite, with the exception of a few crystals residing in sinuous networks (Fig. 11). Using the mass balance approach of Campbell and Murck (1993), orthopyroxene from 38 m of leuconorite would need to be consumed to produce a 2-cm-thick chromitite (80% chromite with 40 wt.% Cr_2O_3) at 50% Cr_2O_3 extraction, while alternatively only 23 m of 60B1:40B2 melt is required to form that same 2-cm-thick chromitite. In the absence of evidence for cumulate melting to this degree (*i.e.*, the anorthosite is relatively thin at the subject locality), it would seem that replenishing melts exert the dominant control on chromite crystallization, which may be later bolstered by Cr^{3+} and Al^{3+} liberated from the resident cumulates. Our thermodynamic modelling shows that residual Cr-spinel is produced in each scenario of footwall reconstitution, particularly in water-rich scenarios (Fig. 13) and that Cr-spinel will saturate in the replenishing melt shortly after orthopyroxene, further supporting a potential dual origin for the lower chromitite.

As described in other studies (Hulbert and Von Gruenewaldt 1985; Vukmanovic *et al.* 2013; Yudovskaya *et al.* 2019) and demonstrated in the bimodal CSD profile (Fig. 6E, F), the lower chromitite of the Merensky Reef hosts two chromite populations - blocky and amoeboidal chromite (Fig. 6). Blocky crystals are devoid of composite inclusions (*i.e.*, grain porosity) and lack evidence for internal misorientation, whereas amoeboidal crystals host abundant composite inclusions and display evidence for a significant degree of internal misorientation. Hulbert and Von Gruenewaldt (1985) proposed that amoeboidal crystals could form through solid-state sintering of initially isolated crystals within a reactive Mg-rich liquid. While sintering is an important postcumulus process in layered intrusions (Hunt *et al.* 2021), the textural (Fig. 6) and chemical (Fig. 7, 8) characteristics of the studied chromite crystals are consistent with the amoeboidal crystals being single crystallographic entities that must have been subsequently reworked by some process.

In a previous study, Vukmanovic *et al.* (2013) postulated that amoeboidal crystals are recrystallized dendritic crystals that initially formed via supercooling near the interface between hot replenishing melt and cool resident cumulates. The misorientation recorded in the crystal lattices of amoeboidal crystals was ascribed to plastic deformation driven by compaction. Our sample of the Merensky Reef displays pristine magmatic textures in its footwall (Figs. 2, 4, and 9) and records no evidence for significant plastic deformation. Observations of chromite behavior during the plastic deformation of chromitiferous peridotites suggest that deformation concentrates in the less competent silicates, leaving chromite relatively undeformed (Holtzman *et al.* 2003; Xiong *et al.* 2017). If plastic deformation was the sole cause of the observed internal misorientation in crystals of the lower chromitite, deformation would have disproportionately concentrated in the silicate oikocrysts. Although the oikocrysts do show some internal misorientation and deformation twins (Fig. 5), taken with their well-defined CPO, these observations are consistent with only small degrees of compaction that is insufficient to explain misorientation in the amoeboidal chromite crystals. Studies of experimental growth of dendrites and skeletal chromite in ophiolites both demonstrate that misorientation in chromite crystals may result from catastrophic crystal growth (Sémoroz *et al.* 2001; Griffiths *et al.* 2023; Henry *et al.* 2024), which fits the context of the Merensky Reef (Vukmanovic *et al.* 2013). We concur with Vukmanovic *et al.* (2013) that amoeboidal chromite crystals initially formed as skeletal crystals that grew rapidly at the interface between hot replenishing melt and cool resident cumulates. The amoeboidal shape arises during a subsequent episode of dissolution-reprecipitation where any misorientation is an artefact of the initial skeletal state (*cf.* Yudovskaya *et al.* 2019). This episode of dissolution-reprecipitation may also contribute to the formation of the blocky chromite population.

Chemical diffusion and evidence for evolved trapped liquid in the reef

Cumulus orthopyroxene crystals adjacent to chromite (Fig. 3A-B) record relatively high $Mg\#_{opx}$ values and lower Cr concentrations. This compositional change is consistent with subsolidus Fe^{2+}-Mg^{2+} and Cr^{3+}-Al^{3+} exchange between chromite and orthopyroxene (Irvine 1967; Sack 1982; Hatton and Von Gruenewaldt 1985; Eales and Reynolds 1986). Although not quantitative, this is broadly consistent with the observed upward increase in chromite Cr# and Mg# values throughout the lower chromitite (Fig. 7), where those relatively Mg- and Al-poor crystals in the uppermost portion have compositional similarities with upper chromitite crystals (Fig. 8). The upper chromitite crystals and those form the uppermost part of the lower chromitite are relatively Ti-rich and associated with abundant accessory rutile (Fig. 7).

With that being said, a high-resolution element map of an amoeboidal chromite at the plagioclase-orthopyroxene oikocryst grain boundary reveals no systematic chemical changes with crystal shape or proximity to orthopyroxene (Fig. 7D). In conclusion, postcumulus diffusion likely augmented chemical gradations in the Merensky chromitite, yet it remains plausible that these chemical gradations relate to primary crystal growth. For example, Ti could diffuse between orthopyroxene and chromite;

however, there is no correlative Ti-depletion in orthopyroxene and tetravalent elements diffuse relatively slowly. The relatively Ti-rich chromite and abundance of accessory rutile are better interpreted as having crystallized from, or interacted with, relatively evolved trapped liquid, which itself may have been liberated from the noritic floor rocks. Poikilitic orthopyroxene in the footwall leuconorite has 1000-1500 ppm Ti (highest in the rims), which when liberated together with Ti from accessory clinopyroxene and chromite (Fig. 11A) might be sufficient to explain the observed Ti distribution. Of further note is that clinopyroxene oikocrysts in the upper portion of the footwall anorthosite contain greater Ti concentrations (~ 0.5 wt.%) than intercumulus clinopyroxene of the Lower Critical Zone (Godel *et al.* 2011).

As predicted in thermodynamic forward models, melts liberated from the footwall may be initially evolved and potentially rich in volatile species. Previous authors have remarked on the occurrence of hydrous accessory phases and occasional graphite in the reef (Ballhaus 1988; Boudreau *et al.* 1986; Li *et al.* 2005), and phlogopite is a common accessory phase in the presently studied rocks, even partially bounding the upper chromitite (Fig. 6B). This observation combined with the relatively Al- and Mg-poor nature of the upper chromitite crystals (Fig. 8A; Barnes *et al.* 2022) is consistent with the coexistence of an evolved trapped melt. Magmatic differentiation would produce a trend of upward decreasing Cr# and Mg# values of chromite, as observed in Lower Zone chromitites (Hatton and von Gruenewaldt 1985; Scoon and Teigler 1995; Naldrett *et al.* 2009). Conversely, in Merensky Reef and UG2 chromitites, Cr# values of chromite crystals as well as Ti, V, and Fe^{3+} concentrations increase with decreasing Mg# values (Fig. 8; Li *et al.* 2005; Vukmanovic *et al.* 2013; Zaccarini *et al.* 2021). This has been interpreted as a product of postcumulus re-equilibration with trapped liquid (Hatton and von Gruenewaldt 1985; Eales and Reynolds 1986; Yudovskaya and Kinnaird 2010; Barnes *et al.* 2022), whereby aliquots of trapped melts may have been preserved as composite inclusions hosted within amoeboidal chromite (Li *et al.* 2005).

A note on the relative timing of the deposition of the hanging-wall pyroxenite

Several past authors have argued that the hanging-wall pyroxenite was deposited by some mechanism prior to the formation of the Merensky Reef (Boudreau *et al.* 1986; Nicholson and Mathez 1991; Hayes *et al.* 2024). However, evidence from the present study is inconsistent with this conclusion. Firstly, the euhedral crystal shapes, well-defined CPO, and undeformed nature of the cumulus orthopyroxene crystals in the studied hanging-wall pyroxenite are consistent with the settling of cumulus crystals from an overlying melt column, which in turn is consistent with the thickening of this unit in pothole-reef facies (Ballhaus 1988; Roberts *et al.* 2007). Secondly, the concentration of sulfides directly above the upper chromitite (*i.e.*, at the base of the hanging-wall pyroxenite; Viljoen 1999; Smith *et al.* 2004; Smith *et al.* 2021) is consistent with the concomitant deposition of cumulus orthopyroxene and sulfide melt, with the latter having undergone some degree of percolation that was hindered by the presence of a pre-existing upper chromitite (*e.g.*, Godel *et al.* 2006). Thirdly, the Merensky pegmatoid and lower chromitite are locally truncated by the hanging-wall pyroxenites (Latypov *et al.* 2015). Fourthly, whole-rock incompatible trace element concentrations peak directly above the peaks in chalcophile metals (Cawthorn 1996; Wilson *et al.* 1999; Cawthorn and Boerst 2006), which has been ascribed to the upward displacement of silicate liquid by down-going sulfide melts and, thus, exchange between the reef interval and the directly overlying cumulates.

Anorthosite formation by replenishment-driven footwall reconstitution with implications for the formation of the Merensky reef sequence

It is proposed that the leuconorite in the footwall of the Merensky Reef formed through the gravitational accumulation of plagioclase and orthopyroxene from a quiescent melt (Fig. 14A). This is consistent with the weakly laminated and undeformed tabular plagioclase crystals that record negligible lineation (Fig. 2). The leucocratic nature of the upper portion of so-called cyclic units likely reflects the difference in settling rates between these phases and, as such, the resident cumulates may have been locally anorthositic (Cawthorn 2002). These resident cumulates were later eroded during an episode of chamber replenishment along the base of the resident magma column, forming the Merensky unconformity (Fig. 14B; Eales 1988; Cawthorn and Boerst 2006; Latypov *et al.* 2022). Chromite must have been the liquidus phase of this replenishing melt.

At the study location, reaction between replenishing melt(s) and resident cumulates is recorded in the upper few centimeters of the footwall (*i.e.*, the footwall anorthosite). The first partial melts liberated from the footwall leuconorite were likely to be relatively volatile-rich and with some Al^{3+} and Cr^{3+} released during the eutectic melting plagioclase and orthopyroxene (O'Driscoll *et al.* 2009; Scoon and Costin 2018; Schannor *et al.* 2018). The introduction of these components to the overlying melt column triggered Cr-supersaturation (Ballhaus 1988), and the *in situ* crystallization of skeletal chromite (Vukmanovic *et al.* 2013). Some sulfide droplets nucleated on these skeletal chromite crystals (Fig. 14C; Barnes *et al.* 2021). The microtextures of amoeboidal chromite are consistent with dissolution-reprecipitation of originally skeletal crystals, which demand a period of Cr-undersaturation perhaps triggered by a subsequent influx of initially Cr-undersaturated melt (Fig. 14D; Yudovskaya *et al.* 2019). The conversion of skeletal to amoeboidal crystals resulted in the entombment of affixed sulfide droplets (Holwell *et al.* 2011; Hutchinson *et al.* 2015) and evolved interstitial melt (Ballhaus and Stumpfl 1986; Li *et al.* 2005; Vukmanovic *et al.* 2013), that itself may represent partial melt liberated from the underlying cumulates. A portion of blocky chromite crystals may form during the reconstitution of skeletal crystals and (or) subsequently as the overlying melt once again becomes Cr-saturated (Fig. 14E).

Following the dissolution-reprecipitation of chromite crystals, sulfide melt percolates downward through the nascent lower chromitite and into the porous footwall (Figs. 11 and 14E; Cawthorn 1999; Naldrett *et al.* 2009; Smith *et al.* 2021). The sulfide melt may only percolate as far down as permitted by the reaction, displacing relatively buoyant evolved trapped melt upwards *en route*. This is consistent with the termination of sinuous channels comprising sulfides, silicates, and very fine-grained chromite at the base of the footwall anorthosite (Fig. 11; Smith *et al.* 2021). The upward-strengthening fabric observed in footwall cumulus plagioclase (Fig. 10) is interpreted as the result of local reordering of tabular crystals in response to the removal of intercumulus liquid (Jerram *et al.* 1996; O'Driscoll *et al.* 2010). However, trapped intercumulus melts were not fully removed from the footwall, where those trapped at the leuconorite-anorthosite transition (*i.e.*, reaction front) chemically equilibrated with relatively poikilitic orthopyroxene (Figs. 11 and 12).

Meanwhile, in the overlying melt, cumulus orthopyroxene and blocky chromite are accumulating above the nascent lower chromitite (Fig. 14E). The indentation of cumulus orthopyroxene causes the mm-scale undulations observed at the upper contact of the lower chromitite (ESM 3vi; Figs. 2 and 5 of Smith *et al.*

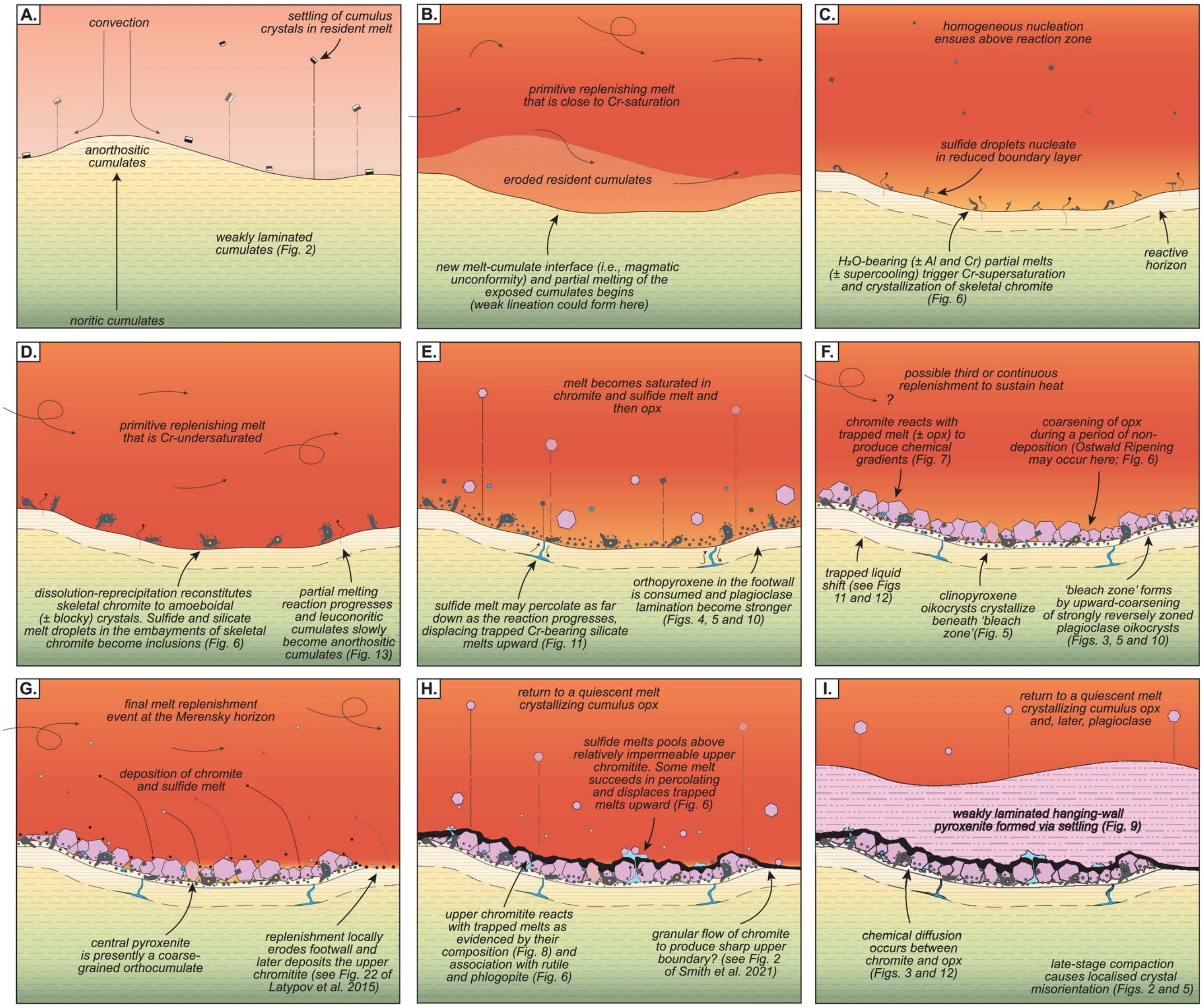

Fig. 14. Schematic model for the formation of the Merensky Reef (Rustenburg facies) and its footwall anorthosite. Full details are outlined in *Section* 5.7. **A.** Deposition of leuconoritic cumulates by gravitational settling of cumulus silicates in a quiescent melt. **B-C.** Basal influx(es) of relatively primitive melt that erodes and partially melts the resident leuconoritic cumulates. Skeletal chromite (± sulfide melt) crystallizes during this reaction. **D-E.** Replenishment by Cr-undersaturated melt triggers dissolution-reprecipitation of skeletal chromite. This melt later deposits chromite, sulfide melt, and then orthopyroxene, where the sulfide melt percolates down into the now-porous footwall cumulates. Partial melting and the resulting modification of the mineral composition of the residue in the footwall continues. **F.** Cumulus orthopyroxene and plagioclase coarsen during an episode of non-deposition and sustained heat brought about by continuous (or subsequent) replenishment. **G.** A final episode of melt replenishment locally erodes the footwall cumulates and deposits the upper chromitite (± sulfide melt). **H-I.** Sulfide melt and then cumulus orthopyroxene settle above the upper chromitite, forming the hanging-wall pyroxenite, where some sulfide melt percolates downward into the orthocumulate central pyroxenite.

2021). A period of non-deposition must have ensued to facilitate the coarsening of this cumulus orthopyroxene by crystal aging (Fig. 14F; Cawthorn and Boerst 2006). This may have occurred when the melt that would deposit the upper chromitite replenished the chamber (Vukmanovic *et al.* 2013), supplying the heat needed to prolong the interaction between cumulus orthopyroxene, the upper portion of the lower chromitite (Fig. 7), and trapped intercumulus melt that was once part of the footwall. The coarsening orthopyroxene encapsulated surrounding chromite crystals (ESM 3vi; Fig. 3C of Cawthorn and Boerst 2006) and grew downwards into the lower chromitite (Fig. 5A). It is around this time that the anorthosite "bleach zone" formed (Nicholson and Mathez 1991), whereby cumulus plagioclase beneath the lower chromitite coarsened upward into it (Fig. 5B-C; Maier and Barnes 2024). This process (described as 'capping' by Kerr and Tait 1986) would have discontinued chemical communication between the footwall and overlying melt, where evolved intercumulus melt would be trapped beneath this layer. This explains the relatively Ti-rich and deformed clinopyroxene oikocrysts present beneath the "bleach zone" (Fig. 5). In the "bleach zone", plagioclase is strongly reversely zoned (Smith *et al.* 2021, 2023; Maier *et al.* 2021b; Latypov *et al.* 2023), whereas in the lower chromitite, the 'reverse zoning' manifests from chromite-to-chromite (*i.e.,* not rim-core-rim; Fig. 3C; Latypov *et al.* 2023). The zoning is ascribed to the preferential leaching of Na by Si-undersaturated intercumulus melts (Ballhaus and Ryan 1995; Marsh *et al.* 2021; Smith *et al.* 2023), perhaps exacerbated by the electrochemical diffusion of Na^+ ions into the overlying magma (Veksler *et al.* 2015).

A final replenishment of Cr-saturated melt occurs, which locally erodes the existing reef stratigraphy (Fig. 14G; Fig. 22 of

Latypov *et al.* 2015). Blocky chromite crystals (± sulfide melt) are deposited at the base of the melt column and sink downwards into the coarse-grained orthopyroxene interstices (Fig. 2 of Smith *et al.* 2021). The overlying melt is saturated in sulfide melt (± cumulus orthopyroxene) and this melt begins to accumulate above the upper chromitite, which acted as a trap (Godel *et al.* 2006). This is consistent with relatively high proportions of sulfide melt observed in the lowermost few centimeters of the hanging-wall pyroxenite (Fig. 6B; Viljoen 1999; Smith *et al.* 2004; Beukes *et al.* 2016; Smith *et al.* 2021). Sulfide melt does eventually breach the upper chromitite (Fig. 14H), displacing trapped melt upwards, consistent with the elevated bulk-rock incompatible element concentrations recorded above this sulfide-rich horizon at Rustenburg (Wilson *et al.* 1999). Moreover, the composition of chromite in the upper chromitite reflects re-equilibration with these trapped melts (Fig. 8; Barnes *et al.* 2022), which is circumstantially supported by the abundance of accessory phlogopite and rutile (Figs. 6B and 7). With no further replenishment episodes, the overlying melt returns to normality, depositing undeformed cumulus orthopyroxene that records a weak lamination (Figs. 9 and 14I). Late-stage compaction was responsible for the localized misorientation observed silicate minerals (Figs. 2 and 5).

CONCLUSION

In the western lobe of the Bushveld Complex, the Merensky Reef is typically underlain by leuconorite and anorthosite. This study proposes that the anorthosite formed when resident leuconoritic cumulates were partially molten by an influx of relatively primitive replenishing melt. The contact between the leuconorite and anorthosite is marked by: (1) relatively increased abundance of intercumulus pyroxenes and accessory phases; (2) complex zoning profiles of cumulus plagioclase; (3) relatively low Mg#$_{opx}$ values, interpreted to be the result of trapped liquid shift. Although fabrics in the footwall are broadly consistent with the gravitational settling of cumulus silicates, plagioclase fabric indices strengthen with proximity to the reef. This is interpreted to result from the progressive removal of intercumulus phases and consequent reordering of cumulus plagioclase. Our data concur with previous authors suggesting that the amoeboidal chromite crystals in the lower chromitite initially formed as skeletal crystals that were subsequently reworked during an episode of dissolution-reprecipitation. The sulfide-rich sinuous networks that traverse the anorthosite formed when sulfide melt percolated into the reconstituted floor rocks. Sulfide melt percolation aided the upward displacement of trapped silicate melt, leading to the introduction of potentially volatile- and Cr-bearing silicate melts to the level of the nascent Merensky Reef. These interpretations are supported by thermodynamic models which demonstrate that replenishment-driven reconstitution of leuconoritic cumulates can trigger formation of a range of footwall lithologies, including anorthosite, norite, olivine norite, troctolite, and orthopyroxenite depending on the nature of the original floor rocks, the water content of the system, and the degree of interaction between the resident cumulates and replenishing melt.

ACKNOWLEDGEMENTS

Anthony Oldroyd is thanked for producing the thick sections. Hadrien Henry acknowledges CNRS funds. Stephen J. Barnes is thanked for providing insightful and constructive comments that improved the manuscript prior to submission. Zhuo-sen Yao is thanked for bringing the experimental works of R.C. Kerr and S.R. Tait to the attention of the authors. Rais Latypov, Ben Hayes, and one anonymous reviewer are thanked for their thorough and constructive reviews that helped to improve the manuscript. Christina Yan Wang is thanked for their editorial handling of this contribution.

DATA AVAILABILITY STATEMENT

The full dataset used in this study is tabulated in the manuscript, reported in the supplementary materials, and available for free download via the CSIRO Digital Access Portal at https://doi.org/10.25919/rgb7-ch54.

REFERENCES

Arndt, N., Jenner, G., Ohnenstetter, M., Deloule, E. & Wilson, A. H. (2005). Trace elements in the Merensky reef and adjacent norites Bushveld complex South Africa. *Mineralium Deposita* **40**, 550–575. https://doi.org/10.1007/s00126-005-0030-x.

Bachmann, F., Hielscher, R. & Schaeben, H. (2010) Texture analysis with MTEX–free and open-source software toolbox. In: *Solid State Phenomena*. Trans Tech Publ, pp.63–68.

Baker, S. R. & Boudreau, A. E. (2019). The influence of the thick banded series anorthosites on the crystallization of the surrounding rock of the Stillwater complex, Montana. *Contrib to Mineral Petrol* **174**, 1–14.

Ballhaus, C. G. (1988). Potholes of the Merensky reef at Brakspruit shaft, Rustenburg platinum mines; primary disturbances in the magmatic stratigraphy. *Economic Geology* **83**, 1140–1158. https://doi.org/10.2113/gsecongeo.83.6.1140.

Ballhaus, C. G. & Stumpfl, E. F. (1986). Sulfide and platinum mineralization in the Merensky reef: evidence from hydrous silicates and fluid inclusions. *Contributions to Mineralogy and Petrology* **94**(2), 193–204. https://doi.org/10.1007/BF00592936.

Ballhaus, C. G. & Ryan, C. G. (1995). Platinum-group elements in the Merensky reef. I. PGE in solid solution in base metal sulfides and the down-temperature equilibration history of Merensky ores. *Contributions to Mineralogy and Petrology* **122**, 241–251. https://doi.org/10.1007/s004100050124.

Barnes, S. J. (1986a). The effect of trapped liquid crystallization on cumulus mineral compositions in layered intrusions. *Contrib to Mineral Petrol* **93**, 524–531. https://doi.org/10.1007/BF00371722.

Barnes, S. J. (1986b). The distribution of chromium among orthopyroxene, spinel and silicate liquid at atmospheric pressure. *Geochimica et Cosmochimica Acta* **50**, 1889–1909. https://doi.org/10.1016/0016-7037(86)90246-2.

Barnes, S.-J. & Maier, W. D. (2002). Platinum-group element distributions in the Rustenburg layered suite of the Bushveld complex, South Africa. *Geol geochemistry Mineral Miner Benef Platinum-gr Elem Canad Inst Min Met Petro CIM Sp* **54**, 431–458.

Barnes, S.-J., Maier, W. D. & Curl, E. A. (2010). Composition of the marginal rocks and sills of the Rustenburg layered suite, Bushveld complex, South Africa: implications for the formation of the platinum-group element deposits. *Economic Geology* **105**, 1491–1511. https://doi.org/10.2113/econgeo.105.8.1491.

Barnes, S.-J., Mansur, E. T., Maier, W. D. & Prevec, S. A. (2022). A comparison of trace element concentrations in chromite from komatiites, picrites, and layered intrusions: implications for the formation of massive chromite layers. *Canadian Journal of Earth Sciences* **60**, 97–132.

Barnes, S. J., Mole, D. R., Le Vaillant, M., Campbell, M. J., Verrall, M. R., Roberts, M. P. & Evans, N. J. (2016). Poikilitic textures, Heteradcumulates and zoned orthopyroxenes in the Ntaka ultramafic complex, Tanzania : implications for crystallization mechanisms of Oikocrysts. *Journal of Petrology* **57**, 1171–1198. https://doi.org/10.1093/petrology/egw036.

Barnes, S. J., Ryan, C., Moorhead, G., Latypov, R., Maier, W. D., Yudovskaya, M., Godel, B., Schoneveld, L. E., Le Vaillant, M. & Pearce, M. B. (2021). Spatial association between platinum minerals and magmatic sulfides imaged with the Maia mapper and implications for the origin of the chromite-sulfide-PGE association. *The Canadian Mineralogist* **59**, 1775–1799. https://doi.org/10.3749/canmin.2000100.

Beukes, J. J., Gauert, C. D. K. & Giebel, R. J. (2016). Cryptic mineral variation and PGE distribution in the Merensky Reef and its discontinuous mela-gabbronoritic hanging wall ("Brown Sugar Norite"-BSN) at Two Rivers Platinum Mine, Eastern Bushveld Complex, South Africa. *South African Journal of Geology* **119**(1), 243–272.

Bohrson, W. A., Spera, F. J., Ghiorso, M. S., Brown, G. A., Creamer, J. B. & Mayfield, A. (2014). Thermodynamic model for energy-constrained open-system evolution of crustal magma bodies undergoing simultaneous recharge, assimilation and crystallization: the magma chamber simulator. *Journal of Petrology* **55**, 1685–1717. https://doi.org/10.1093/petrology/egu036.

Bohrson, W. A., Spera, F. J., Heinonen, J. S., Brown, G. A., Scruggs, M. A., Adams, J. V., Takach, M. K., Zeff, G. & Suikkanen, E. (2020). Diagnosing open-system magmatic processes using the magma chamber simulator (MCS): part II—trace elements and isotopes. *Contrib to Mineral Petrol* **175**, 1–29. https://doi.org/10.1007/s00410-020-01722-z.

Boorman, S., Boudreau, A. & Kruger, F. J. (2004). The lower zone–critical zone transition of the Bushveld complex: a quantitative textural study. *Journal of Petrology* **45**, 1209–1235. https://doi.org/10.1093/petrology/egh011.

Boudreau, A. (1999). Fluid fluxing of cumulates: the JM reef and associated rocks of the Stillwater complex, Montana. *Journal of Petrology* **40**, 755–772. https://doi.org/10.1093/petroj/40.5.755.

Boudreau, A. E., Mathez, E. A. & McCallum, I. S. (1986). Halogen geochemistry of the Stillwater and Bushveld complexes: evidence for transport of the platinum-group elements by Cl-rich fluids. *Journal of Petrology* **27**(4), 967–986. https://doi.org/10.1093/petrology/27.4.967.

Bunge, H. J. (1982). Texture analysis in materials sciencebutterworths. *London* **11**, L0.

Buntin, T. J., Grandstaff, D. E., Ulmer, G. C. & Gold, D. P. (1985). A pilot study of geochemical and redox relationships between potholes and adjacent normal Merensky reef of the Bushveld complex. *Economic Geology* **80**, 975–987. https://doi.org/10.2113/gsecongeo.80.4.975.

Cameron, E. N. (1970). Compositions of certain coexisting phases in the eastern part of the Bushveld complex. *Geol Soc South Africa, Spec Pap* **1**, 46–58.

Cameron, E. N. (1982). The upper critical zone of the eastern Bushveld complex; precursor of the Merensky reef. *Economic Geology* **77**, 1307–1327. https://doi.org/10.2113/gsecongeo.77.6.1307.

Campbell, I. H. (1986). A fluid dynamic model for the potholes of the Merensky reef. *Economic Geology* **81**, 1118–1125. https://doi.org/10.2113/gsecongeo.81.5.1118.

Campbell, I. H. & Murck, B. W. (1993). Petrology of the G and H chromitite zones in the mountain view area of the Stillwater complex, Montana. *Journal of Petrology* **34**, 291–316. https://doi.org/10.1093/petrology/34.2.291.

Carr, H. W., Kruger, F. J., Groves, D. I. & Cawthorn, R. G. (1999). The petrogenesis of Merensky reef potholes at the Western platinum mine, Bushveld complex: Sr-isotopic evidence for synmagmatic deformation. *Miner Depos* **34**, 335–347. https://doi.org/10.1007/s001260050208.

Cawthorn, R. G. (1996). Re-evaluation of magma compositions and processes in the uppermost critical zone of the Bushveld complex. *Mineralogical Magazine* **60**, 131–148. https://doi.org/10.1180/minmag.1996.060.398.09.

Cawthorn, R. G. (1999). Permeability of the footwall cumulates to the Merensky reef, Bushveld complex. *South African J Geol* **102**, 293–310.

Cawthorn, R. G. (2002). Delayed accumulation of plagioclase in the Bushveld complex. *Mineralogical Magazine* **66**, 881–893. https://doi.org/10.1180/0026461026660065.

Cawthorn RG (2015) The Bushveld Complex, South Africa. In: *Layered intrusions*. Springer, pp 517–587, https://doi.org/10.1007/978-94-017-9652-1_12

Cawthorn, R. G. & Boerst, K. (2006). Origin of the pegmatitic pyroxenite in the Merensky unit, Bushveld complex, South Africa. *Journal of Petrology* **47**, 1509–1530. https://doi.org/10.1093/petrology/egl017.

Cawthorn, R. G. & Walraven, F. (1998). Emplacement and crystallization time for the Bushveld complex. *Journal of Petrology* **39**, 1669–1687. https://doi.org/10.1093/petroj/39.9.1669.

Cawthorn, R. G. & Walsh, K. L. (1988). The use of phosphorus contents in yielding estimates of the proportion of trapped liquid in cumulates of the upper zone of the Bushveld complex. *Mineralogical Magazine* **52**, 81–89. https://doi.org/10.1180/minmag.1988.052.364.07.

Cheadle, M. J. & Gee, J. S. (2017). Quantitative textural insights into the formation of gabbro in mafic intrusions. *Elem An Int Mag Mineral Geochemistry, Petrol* **13**, 409–414.

Eales, H. V. & Cawthorn, R. G. (1996). The Bushveld complex. *Layer intrusions* **15**, 181–229. https://doi.org/10.1016/S0167-2894(96)80008-X.

Eales, H. V., De Klerk, W. J. & Teigler, B. (1990). Evidence for magma mixing processes within the critical and lower zones of the northwestern Bushveld complex, South Africa. *Chemical Geology* **88**, 261–278. https://doi.org/10.1016/0009-2541(90)90093-M.

Eales, H. V., Field, M., de Klerk, W. J. & Scoon, R. N. (1988). Regional trends of chemical variation and thermal erosion in the upper critical zone, western Bushveld complex. *Mineralogical Magazine* **52**, 63–79. https://doi.org/10.1180/minmag.1988.052.364.06.

Eales, H. V., Maier, W. D. & Teigler, B. (1991). Corroded plagioclase feldspar inclusions in orthopyroxene and olivine of the lower and critical zones, Western Bushveld complex. *Mineralogical Magazine* **55**, 479–486. https://doi.org/10.1180/minmag.1991.055.380.17.

Eales, H. V., Marsh, J. S., Mitchell, A. A., de Klerk, W. J., Kruger, F. J. & Field, M. (1986). Some geochemical constraints upon models for the crystallization of the upper critical zone-main zone interval, northwestern Bushveld complex. *Mineralogical Magazine* **50**, 567–582. https://doi.org/10.1180/minmag.1986.050.358.03.

Eales, H. V. & Reynolds, I. M. (1986). Cryptic variations within chromitites of the upper critical zone, northwestern Bushveld complex. *Economic Geology* **81**, 1056–1066. https://doi.org/10.2113/gsecongeo.81.5.1056.

Ehlers, T. A. (2005). Crustal thermal processes and the interpretation of thermochronometer data. *Rev Mineral Geochemistry* **58**, 315–350. https://doi.org/10.2138/rmg.2005.58.12.

Evans, D. M. (2018). Significance of compositional zoning in cumulate chromites of the Kabanga chonoliths, Tanzania. *Mineralogical Magazine* **82**, 675–696. https://doi.org/10.1180/mgm.2018.87.

Ghiorso, M. S. & Sack, R. O. (1995). Chemical mass transfer in magmatic processes IV. A revised and internally consistent thermodynamic model for the interpolation and extrapolation of liquid-solid equilibria in magmatic systems at elevated temperatures and pressures. *Contrib to Mineral Petrol* **119**, 197–212. https://doi.org/10.1007/BF00307281.

Godel, B., Barnes, S.-J. & Maier, W. D. (2006). 3-D distribution of sulphide minerals in the Merensky reef (Bushveld complex, South Africa) and the JM reef (Stillwater complex, USA) and their relationship to microstructures using X-ray computed tomography. *Journal of Petrology* **47**(9), 1853–1872. https://doi.org/10.1093/petrology/egl029.

Godel, B., Barnes, S.-J. & Maier, W. D. (2011). Parental magma composition inferred from trace element in cumulus and intercumulus silicate minerals: an example from the Lower and Lower Critical Zones of the Bushveld Complex, South-Africa. *Lithos* **125**(1–2), 537–552.

Griffiths, T. A., Habler, G., Ageeva, O., Sutter, C., Ferrière, L. & Abart, R. (2023). The origin of lattice rotation during dendritic crystallization of Clinopyroxene. *Journal of Petrology* **64**, egac125. https://doi.org/10.1093/petrology/egac125.

Grobler, D. F., Brits, J. A. N., Maier, W. D. & Crossingham, A. (2019). Litho-and chemostratigraphy of the Flatreef PGE deposit, northern Bushveld complex. *Miner Depos* **54**, 3–28. https://doi.org/10.1007/s00126-018-0800-x.

Hatton, C. J. & Von Gruenewaldt, G. (1985). Chromite from the Swartkop chrome mine; an estimate of the effects of subsolidus reequilibration. *Economic Geology* **80**, 911–924. https://doi.org/10.2113/gsecongeo.80.4.911.

Hayes, B., Maghdour-Mashhour, R., Ashwal, L. D., Smith, A. J., Ueckermann, H. & Vermeulen, J. (2024). Melt infiltration in a crystal mush and pegmatoid formation in the platiniferous Merensky reef, Bushveld complex. *South Africa. Mineralium Deposita*. **60**, 237–259. https://doi.org/10.1007/s00126-024-01278-z.

Henry, H., Kaczmarek, M. A., Ceuleneer, G., Tilhac, R., Griffin, W. L., O'Reilly, S. Y., Grégoire, M. & Le Sueur, E. (2021). The microstructure of layered ultramafic cumulates: case study of the Bear Creek intrusion, trinity ophiolite, California, USA. *Lithos* **388-389**, 106047. https://doi.org/10.1016/j.lithos.2021.106047.

Henry, H., Ceuleneer, G., Proietti, A., Kaczmarek, M. A., Chatelin, T. & de Parseval, P. (2024). How does nodular chromite nucleate and grow? An integrated microstructural and petrological approach. *Journal of Petrology* **65**. https://doi.org/10.1093/petrology/egae061.

Higgins, M. D. (2000). Measurement of crystal size distributions. *American Mineralogist* **85**, 1105–1116. https://doi.org/10.2138/am-2000-8-901.

Holwell, D. A., McDonald, I. & Butler, I. B. (2011). Precious metal enrichment in the Platreef, Bushveld complex, South Africa: evidence from homogenized magmatic sulfide melt inclusions. *Contributions to Mineralogy and Petrology* **161**, 1011–1026. https://doi.org/10.1007/s00410-010-0577-0.

Holness, M. B. (2007). Textural immaturity of cumulates as an indicator of magma chamber processes: infiltration and crystal accumulation in the rum eastern layered intrusion. *Journal of the Geological Society of London* **164**, 529–539. https://doi.org/10.1144/0016-76492006-021.

Holness, M. B., Vukmanovic, Z. & Mariani, E. (2017). Assessing the role of compaction in the formation of adcumulates: a microstructural perspective. *Journal of Petrology* **58**, 643–673. https://doi.org/10.1093/petrology/egx037.

Holtzman, B. K., Kohlstedt, D. L., Zimmerman, M. E., Heidelbach, F., Hiraga, T. & Hustoft, J. (2003). Melt segregation and strain partitioning: implications for seismic anisotropy and mantle flow. *Science* **301**(5637), 1227–1230. https://doi.org/10.1126/science.1087132.

Hulbert, L. J. & Von Gruenewaldt, G. (1985). Textural and compositional features of chromite in the lower and critical zones of the Bushveld complex south of Potgietersrus. *Economic Geology* **80**, 872–895. https://doi.org/10.2113/gsecongeo.80.4.872.

Hunt, E. J., Latypov, R. & Horvath, P. (2018). The Merensky cyclic unit, Bushveld complex, South Africa: reality or myth? *Minerals* **8**, 144. https://doi.org/10.3390/min8040144.

Hunt, E. J., O'Driscoll, B. & Day, J. M. D. (2021). Sintering as a key process in the textural evolution of chromitite seams in layered mafic-ultramafic intrusions. *The Canadian Mineralogist* **59**, 1661–1692. https://doi.org/10.3749/canmin.2100021.

Hutchinson, D., Foster, J., Prichard, H. & Gilbert, S. (2015). Concentration of particulate platinum-group minerals during magma emplacement; a case study from the Merensky reef, Bushveld complex. *Journal of Petrology* **56**(1), 113–159. https://doi.org/10.1093/petrology/egu073.

Irvine, T. N. (1967). Chromian spinel as a petrogenetic indicator: part 2. Petrologic applications. *Canadian Journal of Earth Sciences* **4**, 71–103. https://doi.org/10.1139/e67-004.

Irvine, T. N., Keith, D. W. & Todd, S. G. (1983). The JM platinum-palladium reef of the Stillwater complex, Montana; II, origin by double-diffusive convective magma mixing and implications for the Bushveld complex. *Economic Geology* **78**, 1287–1334. https://doi.org/10.2113/gsecongeo.78.7.1287.

Janoušek, V., Farrow, C. M. & Erban, V. (2024). GCDkit. Mineral: a customizable, platform-independent R-language environment for recalculation, plotting, and classification of electron probe microanalyses of common rock-forming minerals. *American Mineralogist* **109**(9), 1598–1607. https://doi.org/10.2138/am-2023-9032.

Jenkins, M. C. & Mungall, J. E. (2018). Genesis of the peridotite zone, Stillwater complex, Montana, USA. *Journal of Petrology* **59**, 2157–2189. https://doi.org/10.1093/petrology/egy093.

Jenkins, M. C., Mungall, J. E., Zientek, M. L., Butak, K., Corson, S., Holick, P., McKinley, R. & Lowers, H. (2022). The geochemical and textural transition between the reef package and its hanging wall, Stillwater complex, Montana, USA. *Journal of Petrology* **63**, egac053. https://doi.org/10.1093/petrology/egac053.

Jenkins, M. C., Mungall, J. E., Zientek, M. L., Costin, G. & Yao, Z. S. (2021). Origin of the JM reef and lower banded series, Stillwater complex, Montana, USA. *Precambrian Research* **367**, 106457. https://doi.org/10.1016/j.precamres.2021.106457.

Jerram, D. A., Cheadle, M. J., Hunter, R. H. & Elliott, M. T. (1996). The spatial distribution of grains and crystals in rocks. *Contributions to Mineralogy and Petrology* **125**, 60–74. https://doi.org/10.1007/s004100050206.

Kerr, R. C. & Tait, S. R. (1986). Crystallization and compositional convection in a porous medium with application to layered igneous intrusions. *Journal of Geophysical Research: Solid Earth* **91**(B3), 3591–3608. https://doi.org/10.1029/JB091iB03p03591.

Kinnaird, J. A. & McDonald, I. (2018). The northern limb of the Bushveld complex: a new economic frontier. *SEG Spcl. Publ. Met. Miner. Soc.* **21**, 157–177.

Kruger, F. J. & Marsh, J. S. (1985). The mineralogy, petrology, and origin of the Merensky cyclic unit in the western Bushveld complex. *Economic Geology* **80**, 958–974. https://doi.org/10.2113/gsecongeo.80.4.958.

Kruger, W. & Latypov, R. (2021). Magmatic karst reveals dynamics of crystallization and differentiation in basaltic magma chambers. *Scientific Reports* **11**, 7341. https://doi.org/10.1038/s41598-021-86724-y.

Langa, M. M., Jugo, P. J., Leybourne, M. I., Grobler, D. F., Adetunji, J. & Skogby, H. (2021). Chromite chemistry of a massive chromitite seam in the northern limb of the Bushveld igneous complex, South Africa: correlation with the UG-2 in the eastern and western limbs and evidence of variable assimilation of footwall rocks. *Mineralium Deposita* **56**, 31–44. https://doi.org/10.1007/s00126-020-00964-y.

Latypov, R. M., Chistyakova, S., Kaufmann, F. E., Roelofse, F., Kruger, W., Barnes, S. J., Magson, J. & Nicholson, M. (2023). The use of an-content of interstitial plagioclase for testing slurry models for the origin of Bushveld massive chromitites. *Lithos* **460-461**, 107374. https://doi.org/10.1016/j.lithos.2023.107374.

Latypov, R., Chistyakova, S., Barnes, S. J. & Hunt, E. J. (2017). Origin of platinum deposits in layered intrusions by in situ crystallization: evidence from undercutting Merensky reef of the Bushveld complex. *Journal of Petrology* **58**(4), 715–761. https://doi.org/10.1093/petrology/egx032.

Latypov, R. M., Chistyakova, S., Page, A. & Hornsey, R. (2015). Field evidence for the in situ crystallization of the Merensky reef. *Journal of Petrology* **56**, 2341–2372. https://doi.org/10.1093/petrology/egv023.

Latypov, R. M., Chistyakova, S., van der Merwe, J. & Westraat, J. (2019). A note on the erosive nature of potholes in the Bushveld complex. *South African Journal of Geology* **122**(4), 555–560. https://doi.org/10.25131/sajg.122.0042.

Latypov, R. M., Heinonen, J. S. & Chistyakova, S. Y. (2022). Magmatic erosion of high-temperature-melting cumulates in the Bushveld complex by chemical dissolution. *Geosystems and Geoenvironment* **1**, 100077. https://doi.org/10.1016/j.geogeo.2022.100077.

Latypov, R., Chistyakova, S., Costin, G., Namur, O., Barnes, S. & Kruger, W. (2020). Monomineralic anorthosites in layered intrusions are indicators of the magma chamber replenishment by plagioclase-only-saturated melts. *Scientific Reports* **10**(1), 3839. https://doi.org/10.1038/s41598-020-60778-w.

Latypov, R. M., Namur, O., Bai, Y., Barnes, S. J., Chistyakova, S., Holness, M. B., Iacono-Marziano, G., Kruger, W. A., O'Driscoll, B., Smith, W. D., Virtanen, V. J., Wang, C. Y., Xing, C. M. & Charlier, B. (2024). Layered intrusions: fundamentals, novel observations and concepts, and controversial issues. *Earth-Science Rev* **249**, 104653. https://doi.org/10.1016/j.earscirev.2023.104653.

Lee, C. A. (1983). Trace and platinum-group element geochemistry and the development of the Merensky unit of the Western Bushveld complex. *Miner Depos* **18**, 173–190. https://doi.org/10.1007/BF00206207.

Leeb-Du, T. A. (1986). The impala platinum mines. *Inmineral deposits of Southern Africa* , 1091–1106.

Lee, C. A. & Butcher, A. R. (1990). Cyclicity in the Sr isotope stratigraphy through the Merensky and bastard reef units, Atok section, eastern Bushveld complex. *Economic Geology* **85**, 877–883. https://doi.org/10.2113/gsecongeo.85.4.877.

Li, C., Ripley, E. M., Sarkar, A., Shin, D. & Maier, W. D. (2005). Origin of phlogopite-orthopyroxene inclusions in chromites from the Merensky reef of the Bushveld complex, South Africa. *Contrib to Mineral Petrol* **150**, 119–130. https://doi.org/10.1007/s00410-005-0013-z.

Maier, W. D. (1992) *Geochemical and petrological trends in the UG2 – Merensky Unit interval of the Upper Critical Zone in the western Bushveld Complex*Unpublished Ph.D. thesis,. Grahamstown: Rhodes University, p.253.

Maier, W. D., Barnes, S.-J. & Groves, D. I. (2013). The Bushveld complex, South Africa: formation of platinum–palladium, chrome-and vanadium-rich layers via hydrodynamic sorting of a mobilized cumulate slurry in a large, relatively slowly cooling, subsiding magma chamber. *Miner Depos* **48**, 1–56. https://doi.org/10.1007/s00126-012-0436-1.

Maier, W. D. & Barnes, S. J. (2024). Origin of chromitite-anorthosite interlayering in the Bushveld complex. *The Canadian Journal of Mineralogy and Petrology.* **62**, 731–745. https://doi.org/10.3749/2300069.

Maier, W. D., Barnes, S. J., Muir, D., Savard, D., Lahaye, Y. & Smith, W. D. (2021a). Formation of Bushveld anorthosite by reactive porous flow. *Contrib to Mineral Petrol* **176**, 1–12. https://doi.org/10.1007/s00410-020-01760-7.

Maier, W. D. & Eales, H. V. (1997). Correlation within the UG2-Merensky reef interval of the western Bushveld complex, based on geochemical, mineralogical, and petrological data.

Maier, W. D., Halkoaho, T., Huhma, H., Hanski, E. & Barnes, S. J. (2018). The Penikat intrusion, Finland: geochemistry, geochronology, and origin of platinum–palladium reefs. *Journal of Petrology* **59**, 967–1006. https://doi.org/10.1093/petrology/egy051.

Maier, W. D., Barnes, S. J., Muir, D., Savard, D., Lahaye, Y. & Smith, W. D. (2021b). Formation of Bushveld anorthosite by reactive porous flow. *Contributions to Mineralogy and Petrology.* **176**, 1–12. https://doi.org/10.1007/s00410-020-01760-7.

Mainprice, D., Bachmann, F., Hielscher, R. & Schaeben, H. (2015). Descriptive tools for the analysis of texture projects with large datasets using MTEX: strength, symmetry and components. *Geol Soc London, Spec Publ* **409**, 251–271. https://doi.org/10.1144/SP409.8.

Marsh, B. D. (1988). Crystal size distribution (CSD) in rocks and the kinetics and dynamics of crystallization: I. *Theory. Contributions to Mineralogy and Petrology.* **99**, 277–291. https://doi.org/10.1007/BF00375362.

Marsh, J. S., Pasecznyk, M. J. & Boudreau, A. E. (2021). Formation of chromitite seams and associated anorthosites in layered intrusion by reactive volatile-rich fluid infiltration. *Journal of Petrology* **62**. https://doi.org/10.1093/petrology/egaa109.

Mathez, E. A. (1995). Magmatic metasomatism and formation of the Merensky reef, Bushveld complex. *Contributions to Mineralogy and Petrology* **119**(2), 277–286. https://doi.org/10.1007/BF00307287.

Mathez, E. A., Hunter, R. H. & Kinzler, R. J. (1997). Petrologic evolution of partially molten cumulate: the Atok section of the Bushveld complex. *Contrib to Mineral Petrol* **129**, 20–34. https://doi.org/10.1007/s004100050320.

Mitchell, A. A. & Scoon, R. N. (2007). The Merensky reef at Winnaarshoek, eastern Bushveld complex: a primary magmatic hypothesis based on a wide reef facies. *Economic Geology* **102**, 971–1009. https://doi.org/10.2113/gsecongeo.102.5.971.

Mitchell, A. A., Scoon, R. N. & Sharpe, M. R. (2019, 2019). The upper critical zone in the Swartklip sector, north-western Bushveld complex, on the farm Wilgerspruit 2JQ: II. Origin by intrusion of ultramafic sills with concomitant partial melting of host norite-anorthosite cumulates. *South African J Geol* **122**, 143–162. https://doi.org/10.25131/sajg.122.0011.

Mudd, G. M., Jowitt, S. M. & Werner, T. T. (2018). Global platinum group element resources, reserves and mining–a critical assessment. *Science of the Total Environment.* **1**(622), 614–625.

Mungall, J. E., Kamo, S. L. & McQuade, S. (2016). U–Pb geochronology documents out-of-sequence emplacement of ultramafic layers in the Bushveld igneous complex of South Africa. *Nature Communications* **7**, 1–13. https://doi.org/10.1038/ncomms13385.

Naldrett, A. J., Gasparrini, E. C., Barnes, S. J., Von Gruenewaldt, G. & Sharpe, M. R. (1986). The upper critical zone of the Bushveld complex and the origin of Merensky-type ores. *Economic Geology* **81**, 1105–1117. https://doi.org/10.2113/gsecongeo.81.5.1105.

Naldrett, A. J., Wilson, A. H., Kinnaird, J. A. & Chunnett, G. (2009). PGE tenor and metal ratios within and below the Merensky reef, Bushveld complex : implications for its genesis. *American Mineralogist* **50**, 625–659. https://doi.org/10.1093/petrology/egp015.

Nicholson, D. M. & Mathez, E. A. (1991). Petrogenesis of the Merensky reef in the Rustenburg section of the Bushveld complex. *Contrib to Mineral Petrol* **107**, 293–309. https://doi.org/10.1007/BF00325100.

O'Driscoll, B., Donaldson, C. H., Daly, J. S. & Emeleus, C. H. (2009). The roles of melt infiltration and cumulate assimilation in the formation of anorthosite and a Cr-spinel seam in the rum eastern layered intrusion, NW Scotland. *Lithos* **111**, 6–20. https://doi.org/10.1016/j.lithos.2008.11.011.

O'Driscoll, B., Emeleus, C. H., Donaldson, C. H. & Daly, J. S. (2010). Cr-spinel seam petrogenesis in the rum layered suite, NW Scotland: cumulate assimilation and in situ crystallization in a deforming crystal mush. *Journal of Petrology* **51**, 1171–1201. https://doi.org/10.1093/petrology/egq013.

Paton, C., Hellstrom, J., Paul, B., Woodhead, J. & Hergt, J. (2011). Iolite: freeware for the visualisation and processing of mass spectrometric data. *Journal of Analytical Atomic Spectrometry.* **26**(12), 2508–2518. https://doi.org/10.1039/c1ja10172b.

Reid, D. & Basson, I. J. (2002). Iron-rich ultramafic pegmatite replacement bodies within the upper critical zone, Rustenburg layered suite, Northam platinum mine, South Africa. *Mineralogical Magazine* **66**, 895–914. https://doi.org/10.1180/0026461026660066.

Robb, S. J. & Mungall, J. E. (2020). Testing emplacement models for the Rustenburg layered suite of the Bushveld complex with numerical heat flow models and plagioclase geospeedometry. *Earth and Planetary Science Letters* **534**, 116084. https://doi.org/10.1016/j.epsl.2020.116084.

Roberts, M. D., Reid, D. L., Miller, J. A., Basson, I. J., Roberts, M. & Smith, D. (2007). The Merensky cyclic unit and its impact on footwall cumulates below Normal and regional pothole reef types in the Western Bushveld complex. *Miner Depos* **42**, 271–292. https://doi.org/10.1007/s00126-006-0111-5.

Sack, R. O. (1982). Spinels as petrogenetic indicators: activity-composition relations at low pressures. *Contrib to Mineral Petrol* **79**, 169–186. https://doi.org/10.1007/BF01132886.

Satsukawa, T., Ildefonse, B., Mainprice, D., Morales, L. F. G., Michibayashi, K. & Barou, F. (2013). A database of plagioclase crystal preferred orientations (CPO) and microstructures–implications for CPO origin, strength, symmetry and seismic anisotropy in gabbroic rocks. *Solid Earth* **4**, 511–542. https://doi.org/10.5194/se-4-511-2013.

Schannor, M., Veksler, I. V., Hecht, L., Harris, C., Romer, R. L. & Manyeruke, T. D. (2018). Small-scale Sr and O isotope variations through the UG2 in the eastern Bushveld complex: the role of crustal fluids. *Chemical Geology* **485**, 100–112. https://doi.org/10.1016/j.chemgeo.2018.03.040.

Schurmann, L. W. (1993). The geochemistry and petrology of the upper critical zone of the Boshoek section of the western Bushveld complex. *Bull van Suid-Afrika, Geol opname* .

Scoates, J. S., Wall, C. J., Friedman, R. M., Weis, D., Mathez, E. A. & VanTongeren, J. A. (2021). Dating the Bushveld complex: timing of crystallization, duration of magmatism, and cooling of the World's largest layered intrusion and related rocks. *Journal of Petrology* **62**. https://doi.org/10.1093/petrology/egaa107.

Scoon, R. N. & Costin, G. (2018). Chemistry, morphology and origin of magmatic-reaction chromite stringers associated with anorthosite in the upper critical zone at Winnaarshoek, eastern limb of the Bushveld complex. *Journal of Petrology* **59**, 1551–1578. https://doi.org/10.1093/petrology/egy071.

Scoon, R. N. & Teigler, B. (1995). A new LG-6 chromite reserve at Eerste Geluk in the boundary zone between the central and southern sectors of the eastern Bushveld complex. *Economic Geology* **90**, 969–982. https://doi.org/10.2113/gsecongeo.90.4.969.

Seabrook, C. L., Cawthorn, R. G. & Kruger, F. J. (2005). The Merensky reef, Bushveld complex: mixing of minerals not mixing of magmas. *Economic Geology* **100**, 1191–1206. https://doi.org/10.2113/gsecongeo.100.6.1191.

Sémoroz, A., Durandet, Y. & Rappaz, M. (2001). EBSD characterization of dendrite growth directions, texture and misorientations in hot-dipped Al–Zn–Si coatings. *Acta Materialia* **49**(3), 529–541. https://doi.org/10.1016/S1359-6454(00)00322-0.

Shaw, C. S. J. & Dingwell, D. B. (2008). Experimental peridotite–melt reaction at one atmosphere: a textural and chemical study. *Contrib to Mineral Petrol* **155**, 199–214. https://doi.org/10.1007/s00410-007-0237-1.

Skemer, P., Katayama, I., Jiang, Z. & Karato, S. (2005). The misorientation index: development of a new method for calculating the strength of lattice-preferred orientation. *Tectonophysics* **411**, 157–167. https://doi.org/10.1016/j.tecto.2005.08.023.

Smith, D. S. & Basson, I. J. (2006). Shape and distribution analysis of Merensky reef potholing, Northam platinum mine, Western Bushveld complex: implications for pothole formation and growth. *Miner Depos* **41**, 281–295. https://doi.org/10.1007/s00126-006-0059-5.

Smith, D. S., Basson, I. J. & Reid, D. L. (2004). Normal reef subfacies of the Merensky reef at Northam platinum mine, Zwartklip facies, Western Bushveld complex, South Africa. *The Canadian Mineralogist* **42**, 243–260. https://doi.org/10.2113/gscanmin.42.2.243.

Smith, W. D. & Maier, W. D. (2021). The geotectonic setting, age and mineral deposit inventory of global layered intrusions. *Earth-Science Rev* **220**, 103736. https://doi.org/10.1016/j.earscirev.2021.103736.

Smith, W. D., Maier, W. D., Barnes, S. J., Moorhead, G., Reid, D. & Karykowski, B. (2021). Element mapping the Merensky reef of the Bushveld complex. *Geoscience Frontiers* **12**, 101101. https://doi.org/10.1016/j.gsf.2020.11.001.

Smith, W. D., Maier, W. D., Muir, D. D., Andersen, J. Ø., Williams, B. J. & Henry, H. (2023). New perspectives on the formation of the Boulder bed of the western Bushveld complex, South Africa. *Miner Depos* **58**, 617–638. https://doi.org/10.1007/s00126-022-01150-y.

Van der Merwe, J. & Cawthorn, R. G. (2005). Structures at the base of the upper group 2 chromitite layer, Bushveld complex, South Africa, on karee mine (Lonmin platinum). *Lithos* **83**, 214–228. https://doi.org/10.1016/j.lithos.2005.03.003.

Veksler, I. V., Reid, D. L., Dulski, P., Keiding, J. K., Schannor, M., Hecht, L. & Trumbull, R. B. (2015). Electrochemical processes in a crystal mush: cyclic units in the upper critical zone of the Bushveld complex, South Africa. *Journal of Petrology* **56**, 1229–1250. https://doi.org/10.1093/petrology/egv036.

Vermaak, C. F. (1976). The Merensky reef; thoughts on its environment and genesis. *Economic Geology* **71**(7), 1270–1298. https://doi.org/10.2113/gsecongeo.71.7.1270.

Viljoen, C. F. & Hieber, R. (1986) The Rustenburg Section of Rustenburg Platinum Mine Ltd. with reference to the Merensky Reef. In: *Mineral Deposits of Southern Africa*, pp.1107–1134.

Viljoen, M. J., Theron, J., Underwood, B., Walters, B. M., Weaver, J. & Peyerl, W. (1986a) The Amandelbult section of Rustenburg Platinum Mines Limited, with reference to the Merensky reef. In: *Mineral deposits of southern Africa*, pp.1041–1060.

Viljoen, M. J. (1999). The nature and origin of the Merensky reef of the western Bushveld complex based on geological facies and geophysical data. *South African J Geol* **102**, 221–239.

Viljoen, M. J., Theron, J., Underwood, B., Walters, B. M., Weaver, J. & Peyerl, W. (1986b) The Amandelbult section of Rustenburg Platinum Mines Limited, with reference to the Merensky reef. In: *Mineral deposits of southern Africa*, pp.1041–1060.

Viring, R. G. & Cowell, M. W. (1999). The Merensky reef on Northam platinum limited. *South African J Geol* **102**, 192–208.

Vukmanovic, Z., Barnes, S. J., Reddy, S. M., Godel, B. & Fiorentini, M. L. (2013). Morphology and microstructure of chromite crystals in chromitites from the Merensky reef (Bushveld complex, South Africa). *Contrib to Mineral Petrol* **165**, 1031–1050. https://doi.org/10.1007/s00410-012-0846-1.

Vukmanovic, Z., Holness, M. B., Stock, M. J. & Roberts, R. J. (2019). The creation and evolution of crystal mush in the upper zone of the Rustenburg layered suite, Bushveld complex, South Africa. *Journal of Petrology* **60**, 1523–1542. https://doi.org/10.1093/petrology/egz038.

Wager, L. R. & Brown, G. M. (1968) Layered igneous intrusions. In: *Edinburgh London Oliver Boyd*, pp.1–588.

Wagner, P. A. (1929) The platinum deposits and mines of South Africa. In: *Edinburgh, Oliver and Boyd*, p.326.

Wilson, A. H., Lee, C. A. & Brown, R. T. (1999). Geochemistry of the Merensky reef, Rustenburg section, Bushveld complex: controls on the silicate framework and distribution of trace elements. *Miner Depos* **34**, 657–672. https://doi.org/10.1007/s001260050226.

Xiong, Q., Henry, H., Griffin, W. L., Zheng, J. P., Satsukawa, T., Pearson, N. J. & O'Reilly, S. Y. (2017). High-and low-Cr chromitite and dunite in a Tibetan ophiolite: evolution from mature subduction system to incipient forearc in the neo-Tethyan Ocean. *Contributions to Mineralogy and Petrology* **172**, 1–22. https://doi.org/10.1007/s00410-017-1364-y.

Yao, Z., Mungall, J. E. & Jenkins, M. C. (2021). The Rustenburg layered suite formed as a stack of mush with transient magma chambers. *Nature Communications* **12**, 505. https://doi.org/10.1038/s41467-020-20778-w.

Yudovskaya, M. A. & Kinnaird, J. A. (2010). Chromite in the Platreef (Bushveld complex, South Africa): occurrence and evolution of its chemical composition. *Mineralium Deposita* **45**, 369–391. https://doi.org/10.1007/s00126-010-0276-9.

Yudovskaya, M. A., Costin, G., Shilovskikh, V., Chaplygin, I., McCreesh, M. & Kinnaird, J. (2019). Bushveld symplectic and sieve-textured chromite is a result of coupled dissolution-reprecipitation: a comparison with xenocrystic chromite reactions in arc basalt. *Contrib to Mineral Petrol* **174**, 1–21. https://doi.org/10.1007/s00410-019-1613-3.

Zaccarini, F., Garuti, G., Luvizotto, G. L., de Melo, P. Y. & Singh, A. K. (2021). Testing trace-element distribution and the Zr-based thermometry of accessory rutile from chromitite. *Minerals.* **11**(7), 661. https://doi.org/10.3390/min11070661.

Journal of Petrology, 2025, **66**, egaf015
https://doi.org/10.1093/petrology/egaf015
Original Manuscript